

## RADIO POLARIZATION FROM THE INNER GALAXY AT ARC-MINUTE RESOLUTION

B. M. GAENSLER<sup>1,6</sup>, JOHN M. DICKEY<sup>2</sup>, N. M. MCCLURE-GRIFFITHS<sup>2</sup>, A. J. GREEN<sup>3</sup>,  
 M. H. WIERINGA<sup>4</sup> AND R. F. HAYNES<sup>5</sup>

*Accepted by the Astrophysical Journal*

### ABSTRACT

The Southern Galactic Plane Survey (SGPS) is an H I and 1.4-GHz continuum survey of the 4th quadrant of the Galaxy at arcmin resolution. We present here results on linearly polarized continuum emission from an initial 28-square-degree Test Region for the SGPS, consisting of 190 mosaiced pointings of the Australia Telescope Compact Array, and covering the range  $325.5 < l < 332.5$ ,  $-0.5 < b < +3.5$ . Complicated extended structure is seen in linear polarization throughout the Test Region, almost all of which has no correlation with total intensity. We interpret the brightest regions of polarized emission as representing intrinsic structure in extended polarization, most likely originating in the Crux spiral arm at a distance of 3.5 kpc; fainter polarized structure is imposed by Faraday rotation in foreground material. Two large areas in the field are devoid of polarization. We argue that these voids are produced by foreground H II regions in which the magnetic field is disordered on scales of  $\sim 0.1-0.2$  pc. We also identify a depolarized halo around the H II region RCW 94, which we suggest results from the interaction of the H II region with a surrounding molecular cloud.

*Subject headings:* H II regions: general – H II regions: individual: (RCW 94) – ISM: magnetic fields – polarization – radio continuum: general – radio continuum: ISM

### 1. INTRODUCTION

Soon after linear polarization was first detected from celestial radio sources, it became apparent that the entire Galactic Plane was a significant source of polarized emission (Seeger & Westervhout 1961). There appear to be at least two components to this emission (e.g. Junkes, Fürst, & Reich 1987; Duncan et al. 1997a): polarization from discrete supernova remnants (SNRs), and a diffuse polarized background produced by the interaction of the relativistic component of the interstellar medium (ISM) with the Galactic magnetic field.

In the presence of magnetic fields and free electrons, electromagnetic radiation propagates in two circularly-polarized orthogonal modes of different velocities. Linearly polarized radiation passing through a magneto-ionized medium will thus emerge with its position angle rotated, an effect known as *Faraday rotation* (Faraday 1844; Cooper & Price 1961). If a source emits linear polarization with an intrinsic position angle  $\Theta_0$ , then the measured position angle  $\Theta$  at an observing wavelength  $\lambda$  is given by:

$$\Theta = \Theta_0 + \text{RM} \lambda^2. \quad (1)$$

In this expression, the *rotation measure* (RM), in units of  $\text{rad m}^{-2}$ , is defined by:

$$\text{RM} = K \int B \cos \theta n_e dl, \quad (2)$$

where  $K = 0.81 \text{ rad m}^{-2} \text{ pc}^{-1} \text{ cm}^3 \mu\text{G}^{-1}$ ,  $B$ ,  $\theta$  and  $n_e$  are the magnetic field strength, inclination of the magnetic field to the line of sight and electron density respectively, and the integral is along the line of sight from the observer to the source.

Faraday rotation can be a powerful probe of Galactic sources, and has been used to determine the magneto-ionic properties of both individual objects (e.g. Heiles & Chu 1980; Matsui et al. 1984) and of the Galaxy as a whole (e.g. Simard-Normandin & Kronberg 1980; Han & Qiao 1994). Extragalactic sources (Clegg et al. 1992), pulsars (Han, Manchester, & Qiao 1999) and extended polarized emission from the entire Galaxy (Spoelstra 1984) have all been used as background sources against which Faraday rotation can be studied. However, with a single-dish telescope all such studies have their limitations — studies of extragalactic sources suffer from confusion in the Galactic Plane, pulsars are of too low spatial density to study specific regions of the sky in detail, and the spatial resolution with which extended emission can be imaged is generally poor.

In more recent years, instruments and techniques have been developed which allow interferometers to map large regions of the sky in polarization. Consequent polarimetric surveys with both the Westerbork and DRAO Synthesis Telescopes do not suffer from any of the problems described above for single-dish observations, and can thus study polarization and Faraday rotation at high spatial resolution. These studies have revealed several unusual features with no counterparts either in total intensity or at any other wavelength (Wieringa et al. 1993; Gray et al. 1998; Gray et al. 1999; Haverkorn, Katgert, & de Bruyn 2000). These results demonstrate that there are components of the ISM which can only be studied through polarimetry.

The above-mentioned surveys have been carried out at high Galactic latitudes and/or in the 2nd Galactic quadrant, and thus provide important information on the magneto-ionic properties of local gas and of the outer Galaxy. However, it is also of considerable interest to study the polarimetric properties of the in-

<sup>1</sup>Center for Space Research, Massachusetts Institute of Technology, 70 Vassar Street, Cambridge, MA 02139; bmg@space.mit.edu

<sup>2</sup>Department of Astronomy, University of Minnesota, 116 Church Street SE, Minneapolis, MN 55455

<sup>3</sup>Astrophysics Department, School of Physics, University of Sydney, NSW 2006, Australia

<sup>4</sup>Australia Telescope National Facility, CSIRO, Locked Bag 194, Narrabri, NSW 2390, Australia

<sup>5</sup>Australia Telescope National Facility, CSIRO, PO Box 76, Epping, NSW 1718, Australia

<sup>6</sup>Hubble Fellow

ner Galaxy, in which there are undoubtedly regions of stronger magnetic fields, higher densities and increased levels of turbulence. The complexity of polarization in this part of the sky has been demonstrated by the spectacular single-dish polarization surveys of Duncan et al. (1997a, 1999), but a full understanding of the emission in these regions requires the higher angular resolution which only an interferometer can provide.

The Australia Telescope Compact Array (ATCA) is ideally suited to such a study. Its antipodean location allows it to observe almost the entire 4th Galactic quadrant, the high polarimetric purity of its receivers ensures that polarized signals are uncontaminated by leakage from total intensity, its mosaicing capability allows it to easily map large parts of the sky, its multi-channel continuum mode allows accurate studies of Faraday rotation, and its compact antenna configurations give it good sensitivity to extended structure. Motivated by these capabilities, we are in the process of mapping the entire Galactic Plane south of declination  $\sim -35^\circ$  in 1.4-GHz polarization; observations are being made simultaneously in the H I line. Together with single-dish H I data being taken with the 64-m Parkes radiotelescope (McClure-Griffiths et al. 2000c), all these data form the *Southern Galactic Plane Survey* (SGPS; Dickey et al. 1999; McClure-Griffiths et al. 2000b)<sup>7</sup>, the ATCA component of which will cover the Galactic coordinates  $253^\circ < l < 358^\circ$ ,  $-1^\circ < b < 1^\circ$ . The polarimetric component of this data-set will have a spatial resolution of  $\sim 1$  arcmin, and a theoretical sensitivity of  $\sim 0.25$  mJy (where 1 jansky =  $10^{-26}$  W m<sup>-2</sup> Hz<sup>-1</sup>).

Before embarking on the full SGPS, we carried out ATCA observations on a small Test Region, covering the range  $325.5 < l < 332.5$ ,  $-0.5 < b < +3.5$ . A preliminary image of this region, at a resolution of  $\sim 5$  arcmin, was presented by Dickey (1997). We present here our entire data-set on polarization from the SGPS Test Region, at the final survey resolution of 1 arcmin. In Section 2 we describe the aspects of SGPS observations and data-reduction relevant to the polarimetric component of the survey, while in Section 3 we present the distribution of polarized emission and of rotation measure which we have determined from these data. In Section 4, we interpret these results in terms of intrinsic polarization and Faraday rotation in the Galactic Plane. The present paper focuses on extended regions of linear polarization; in a separate paper by Dickey et al. (in preparation), we show how the RMs measured towards point sources in the SGPS Test Region can constrain models of the Galactic magnetic field.

## 2. OBSERVATIONS AND REDUCTION

Observations of the SGPS Test Region were made with the Australia Telescope Compact Array (ATCA; Frater, Brooks, & Whiteoak 1992), a synthesis telescope located near Narrabri, NSW, Australia. Details of the observing dates, array configurations and pointing centers for observations of the Test Region will be described in a forthcoming paper by McClure-Griffiths et al. (2000d). All reduction was carried out in the MIRIAD package (Sault & Killeen 1999), using standard techniques unless otherwise specified.

Each antenna of the ATCA receives incident radiation in two orthogonal, linearly polarized modes,  $X$  and  $Y$ . Four polarization spectra,  $XX$ ,  $YY$ ,  $XY$  and  $YX$ , are consequently measured for each correlation. These data are recorded as 32 4-MHz channels across a 128-MHz bandwidth, with a center frequency of 1384 MHz. The ATCA's continuum mode includes an inher-

ent triangular weighting for the lag-spectrum, meaning that alternate channels are redundant; we thus discarded every second channel. We also discarded four channels on either edge of the bandpass because of low signal-to-noise, and removed channels centered on 1376, 1384 and 1408 MHz because of interference (both external and self-generated). The resulting data consisted of nine spectral channels across 96 MHz of bandwidth. Additional editing was then carried out to remove time-ranges and visibilities corrupted by instrumental problems and radio interference.

Flux density and bandpass calibrations were applied to the data using a  $\sim 10$ -min observation, made once each synthesis, of PKS B1934–638, for which we assumed a flux density of 14.94 Jy at 1384 MHz (Reynolds 1994). Variations of the atmospheric gain above each antenna as a function of time were determined using a 3-min observation of either MRC B1438–481 or MRC B1613–586 every  $\sim 100$  minutes. Observations of these calibrators over a wide range in parallactic angle were used also to solve for the instrumental polarization characteristics of each antenna (Sault, Hamaker, & Bregman 1996). The calibrated data were then converted to the four standard Stokes parameters,  $I$ ,  $Q$ ,  $U$  and  $V$ .

The visibilities from all observations were then inverted to produce images of the Test Region using all baselines between 31 m and 765 m, and employing a uniform weighting scheme to minimize sidelobe contributions from strong sources. A mosaiced image of the entire Test Region was formed for each of the nine spectral channels and four Stokes parameters (36 images in total) by linearly combining data from the 190 separate pointings (Cornwell, Holdaway, & Uson 1993; Sault, Staveley-Smith, & Brouw 1996). The four Stokes images for each spectral channel were deconvolved jointly using the maximum entropy algorithm PMOSMEM (Sault, Bock, & Duncan 1999). This approach successfully recovers the large-scale structure measured by the mosaicing process (Ekers & Rots 1979), and also uses the “maximum emptiness” criterion, which allows the Stokes  $Q$ ,  $U$  and  $V$  maps to take on negative values. No constraints were given to the deconvolution process regarding the total flux density in each image or sub-region to be deconvolved. Following deconvolution, each of the 36 images was smoothed with a gaussian restoring beam of FWHM  $87'' \times 67''$ , the major axis being oriented approximately north-south. The images were then re-gridded into Galactic coordinates using a gnomonic (“TAN”) projection (see Greisen & Calabretta 1995 and references therein). Images of linearly polarized intensity,  $L = (Q^2 + U^2)^{1/2}$ , linearly polarized position angle,  $\Theta = \frac{1}{2} \tan^{-1}(U/Q)$ , and uncertainty in position angle,  $\Delta\Theta = \sigma_{Q,U}/2L$ , were then formed from each pair of  $Q$  and  $U$  images, where  $\sigma_{Q,U}$  is the RMS sensitivity in the  $Q$  and  $U$  images. A correction was applied to the  $L$  images to account for the Ricean bias produced when  $Q$  and  $U$  are combined (Killeen, Bicknell, & Ekers 1986). The nine  $L$  maps (one per spectral channel) were then averaged together to make a final image of  $L$  for the entire Test Region. The position angle maps were also corrected so that position angles were relative to Galactic, rather than equatorial, coordinates.

Note that an alternative approach to the data reduction would have been to form a single image for each Stokes parameter using multi-frequency synthesis, whereby the data from all spectral channels are imaged simultaneously (Sault & Wieringa 1994). While this approach results in improved  $u-v$  coverage

<sup>7</sup>see also the SGPS WWW page, at <http://www.astro.umn.edu/~naomi/sgps.html> .

and image fidelity, the resulting images of polarized intensity would suffer from significant depolarization wherever Faraday rotation across the 96-MHz observing bandwidth was significant. By combining information from each channel only after we have formed separate images of  $L$  for each, we reduce the effects of bandwidth depolarization to only what is incurred across each 8-MHz channel.

### 3. RESULTS

#### 3.1. Images of Polarized Intensity

Over most of the field, data at a given position contains contributions from nine adjacent pointings; the resultant theoretical sensitivity in each Stokes parameter is  $\sim 0.5$  mJy beam $^{-1}$ . In a strip of width  $0.5$  around the edge of the field, the sensitivity has a higher value of  $\sim 0.9$  mJy beam $^{-1}$  because the number of adjacent fields is smaller.

A total intensity image is shown in Fig 1. This image, which will be discussed in more detail by McClure-Griffiths et al. (2000d) McClure-Griffiths et al. 2000d), shows a variety of SNRs and H II regions along the Galactic Plane, embedded in more diffuse emission to which the available interferometric spacings are only partially sensitive. Further from the Plane ( $b \gtrsim 1^\circ$ ), only unresolved, presumably background sources are seen. The structure seen in this image is very similar to that seen at 843 MHz and at comparable resolution in the Molonglo Galactic Plane Survey (Fig 4 of Green et al. 1999). For comparison purposes, in Fig 2 we show the total intensity from the 2.4 GHz survey of Duncan et al. (1995), which was carried out with the 64-m Parkes radiotelescope at an angular resolution of  $10.4$ . Although the single-dish observations detect a considerable amount of extended emission to which the interferometer is not sensitive, the same main features are identifiable in each of Figs 1 and 2.

Linearly polarized emission from the SGPS data-set is shown in Figs 3, 4 and 5. Figs 3 and 4 display the intensity of extended linear polarization using two different greyscale ranges, while Fig 5 illustrates the polarization position angle (averaged across the nine spectral channels) for these data.

Five distinct classes of feature can be seen in the ATCA images:

1. Structures in polarization and depolarization corresponding directly to sources seen in total intensity — these features are discussed in more detail in Section 3.3.
2. Diffuse polarization across the entire field of view. Fig 5 demonstrates that this emission is composed of discrete patches, in each of which the position angle of polarization is approximately uniform. However, sudden changes in position angle are seen between one patch and the next.
3. Narrow “canals” of greatly reduced polarization running randomly throughout the diffuse component, best seen in Fig 4.
4. Large “voids” of reduced polarization, several degrees across, most clearly seen in Fig 4. There are two particularly distinct such voids, the outer perimeters of which we have approximated by ellipses in Fig 4: the first of these (henceforth referred to as “void 1”) is approximately circular, centered on approximately  $(l, b) = (332.4, +1.4)$ <sup>8</sup>

with a radius  $1.0 - 1.5$ . The second void (“void 2”) runs along the bottom edge of the field, with center  $(328.2, -0.5)$  and minor-axes in the  $l$  and  $b$  directions of  $\sim 2^\circ$  and  $\sim 1.5$  respectively. Neither void has any counterpart in total intensity, when viewed either with the interferometer (Fig 1) or with a single-dish (Fig 2).

5. Polarized point sources throughout the field of view, best seen in Fig 3.

In Fig 6 we show the linearly polarized intensity from the 2.4 GHz Parkes survey (Duncan et al. 1997a) at a resolution of  $10.4$ , covering the same area as the SGPS Test Region. Some significant similarities and differences can immediately be seen by comparing Figs 3 and 4 with Fig 6.

First, we note that the two voids described above are clearly seen also at 2.4 GHz. In the wider field images presented in Fig 4 of Duncan et al. (1997a), the two voids can be seen to be nearly complete shells.

Duncan et al. (1997a) identified two components in the polarization they detected: bright, extended regions of emission, and fainter regions with a patchy or clumpy morphology. Both components can clearly be seen in Fig 6. The bright emission extends approximately horizontally across the range  $327^\circ < l < 331^\circ$ , with a prominent spur extending away from the plane at  $l = 329^\circ$ . Fainter, patchier emission can be seen over almost all the rest of the field. Generally speaking, most of the bright and extended emission seen at 2.4 GHz is well-correlated with polarized emission seen in our 1.4 GHz data. On the other hand, the fainter patches seen at 2.4 GHz show little correspondence with polarization at 1.4 GHz.

One notable exception to this is in the range  $328.5 < l < 329.5$ ,  $2.0 < b < 3.5$ , where the boundaries of the bright spur seen at 2.4 GHz seem to correspond to a region of low polarization at 1.4 GHz. Meanwhile, the hole in polarization seen just to the right of the 2.4 GHz spur corresponds to bright polarization at 1.4 GHz.

In circular polarization (not shown here), instrumental artifacts can be seen at the positions of the brightest continuum sources, corresponding to leakage from Stokes  $I$  into Stokes  $V$ . The only other source showing emission at more than a level of  $5\sigma$  in both Stokes  $I$  and  $V$  is the pulsar PSR B1557–50 at position  $(330.69, +1.63)$ , which has  $I = 15$  mJy and  $V = -5$  mJy.<sup>9</sup> This is in reasonable agreement with the previously measured value of  $V/I \approx -0.15$  for this source (Han et al. 1998 and references therein).

#### 3.2. Determination of Rotation Measures

At almost every point where linear polarization is detected, the position angle of this polarization varies from channel to channel across the observing band as a result of Faraday rotation. This effect can be used to calculate the rotation measure (RM) of the polarization.

We calculate the RM as a function of position from images of  $\Theta$  and  $\Delta\Theta$  using the MIRIAD task IMRM (Sault & Killeen 1999). The algorithm used by IMRM is as follows (the nine channels being considered in order of decreasing frequency):

1. For each pixel, a function of the form given by Equation (1) is fitted to the values of  $\Theta$ ,  $\Delta\Theta$  and  $\lambda$  corresponding to the first two channels only. This produces an initial estimate of the values of RM and  $\Theta_0$ .

<sup>8</sup>Throughout this paper, we refer to the position of a source with coordinates  $l = l_0$ ,  $b = b_0$  using the notation  $(l_0, b_0)$ .

<sup>9</sup>Circular polarization is defined such that  $V > 0$  corresponds to right-hand circular polarization.

2. These estimates are then used to predict values of  $\Theta$  at the other seven frequencies.
3. Integer multiples of  $\pi$  radians are then added or subtracted to the position angles at the other frequencies in order to make their position angles as close as possible to the predicted values of  $\Theta$ .
4. A least squares fit is then used to solve for RM and  $\Theta_0$  using the data from all nine spectral channels.
5. This RM is subtracted from the data, and steps 1 through 4 are repeated.
6. The RMs determined in the two executions of step 4 are added together to give a final estimate of the RM.

We only carried out this computation at pixels for which the polarized intensity met the criterion  $L > 5\sigma \approx 3 \text{ mJy beam}^{-1}$ , for which the reduced  $\chi^2$  of the least squares fit in Step 3 above satisfied  $\chi_r^2 < 1$ , and which did not correspond to polarized point sources (which are treated separately in Section 3.3.1 below). Using this approach, we were able to calculate a RM for 13% of the  $\sim 9.9 \times 10^5$  pixels in the map; the resulting distribution of RM is shown in Fig 7. The uncertainty in an individual RM measurement depends on signal-to-noise, but is typically in the range  $\Delta\text{RM} = 20\text{--}40 \text{ rad m}^{-2}$ .

It can be seen that the RMs are mostly small and negative — 50% of the RMs have magnitudes smaller than  $\pm 25 \text{ rad m}^{-2}$  and 98% are smaller than  $\pm 100 \text{ rad m}^{-2}$ . The mean RM of the entire region is  $-12.9 \pm 0.1 \text{ rad m}^{-2}$ , with a median of  $-12.7 \text{ rad m}^{-2}$ ; Some RMs of magnitudes of up to  $\pm 400 \text{ rad m}^{-2}$  are seen — these are predominantly on the edges of voids, particularly in the region  $331^\circ < l < 332^\circ$ . In Fig 8 we show RMs towards four representative regions. We have chosen two RMs of small magnitude and two of large magnitude; it can be seen that in all cases the fit to the data is very good, as demanded by the constraint imposed on  $\chi^2$ .

### 3.3. Discrete Structures in Polarization

#### 3.3.1. Compact Sources

It is difficult to identify polarized emission from compact sources in Figs 3 and 4, because of the diffuse polarization which covers most of the field. To look for polarization on small scales, we thus re-imaged the data in  $I$  and in  $L$  as described in Section 2, but only using baselines between 210 m and 765 m. The resulting images are sensitive only to scales smaller than  $\sim 3'$ .

The RMS noise in the resulting  $Q$  and  $U$  images is  $\sim 0.55 \text{ mJy beam}^{-1}$ , and in the corresponding total intensity image is  $\sim 0.8 \text{ mJy beam}^{-1}$ . Adopting a  $5\sigma$  detection threshold, we consider a source to be linearly polarized if its surface brightnesses exceed  $L > 2.75 \text{ mJy beam}^{-1}$  and  $I > 4.0 \text{ mJy beam}^{-1}$ . We only consider sources for which  $L/I \gtrsim 0.005$ , since instrumental leakage can introduce spurious polarization below this level.

With these criteria, we find 21 compact sources showing linear polarization. We determined the rotation measure (RM) of each source using the method described in Section 3.2 above, but relaxing the requirement that  $\chi_r^2 < 1$ . The data and the RM function fitted to them in each case are shown in Fig 9. The 21 sources are listed in Table 1; columns 1 through 7 indicate respectively the source number, the Galactic longitude and latitude of the pixel with the highest linearly polarized intensity,

the values of  $L$  and  $I$  at this pixel, the ratio  $L/I$  for this pixel, and the RM for this pixel.

These sources will not be discussed further here. In an associated paper by Dickey et al. (in preparation), we show how the RMs which we have determined for these sources can be applied to models for the magnetic field structure of the Galaxy.

#### 3.3.2. Supernova Remnants

There are seven SNRs from the catalogue of Green (2000) in the Test Region. While polarization is detected in the direction of all these sources, the presence of significant polarized emission throughout the field makes it difficult to determine whether this polarization is associated with a SNR or just happens to lie along the same line of sight. Only in the case of G327.4+0.4 (Kes 27; Milne et al. 1989) is the morphology of polarized emission correlated with the total intensity from the SNR, and thus likely to be associated with it.

#### 3.3.3. H II Regions

There are  $\sim 30$  radio H II regions within the SGPS Test Region (e.g. Avedisova 1997). Most of these sources are either near the edge of the field, or are projected against void 2, and so it is not possible to determine whether they have any effect on the polarized emission at their positions. However, there is one H II region, RCW 94 (= G326.3+0.8), whose presence is clearly seen in polarization.

The polarization in the direction of RCW 94 is shown in Fig 10. There is bright linearly polarized emission in the vicinity, particularly to the lower-left of the H II region where the surface brightness in polarization is  $5\text{--}10 \text{ mJy beam}^{-1}$ . However, at positions coincident with the interior of the H II region, the polarized intensity is significantly reduced, falling in the range  $3\text{--}5 \text{ mJy beam}^{-1}$ . More notably, an annulus of width  $\sim 5'$  almost completely surrounds RCW 94, in which the level of polarization is reduced even further — in most of this halo no polarization is detected at all, down to a limit of  $\sim 2 \text{ mJy beam}^{-1}$ . Both these effects are demonstrated quantitatively in Fig 11, in which profiles of  $I$  and  $L$  are shown for the slice marked in Fig 10. Both the region of reduced polarization in the interior of RCW 94 and the very low levels of polarization around it can clearly be seen.

Another H II region, G326.7+0.5 is 30 arcmin to the lower-left of RCW 94. Linear polarization in the interior of the source has a mean surface brightness of  $\sim 5 \text{ mJy beam}^{-1}$ , brighter than in the interior of RCW 94 but still approximately half the brightness of the surrounding emission. Although not as striking as for RCW 94, there is possibly a partial halo of very low polarization surrounding G326.7+0.5, most noticeable to the left of the source. This region extends to approximately twice the radius of the H II region.

## 4. DISCUSSION

### 4.1. Interferometric Observations of Faraday Rotation

Before interpreting the diffuse polarized emission seen in the Test Region, it is important to consider what an interferometer detects when it observes polarized emission which has undergone Faraday rotation.

In Appendix A we consider a simple model involving a uniform polarized background, which passes through both a uniform screen of RM  $R_s$  and also a compact cloud of RM  $R_c$ . The background polarization, after passing through the screen,

has its position angle changed, but is still uniform in  $I$ ,  $Q$  and  $U$ . Since the interferometer has no sensitivity to a constant offset in intensity, this component of the emission is not detected. However, the emission passing through the compact cloud emerges with a different polarized position angle from elsewhere. Thus while the emission in Stokes  $I$  is unaffected by passage through the cloud and so remains invisible to the interferometer, structure is produced in  $Q$  and  $U$  on scales to which the interferometer is sensitive.

This polarized emission has two important properties (see Appendix A):

1. A polarized source will be detected at the position of the cloud which has no counterpart in total intensity. The surface brightness of this polarized emission can be up to twice that of the (undetected) uniform polarized background.
2. The measured RM at this position will be equal to  $R_s + R_c/2$ . Thus even though the uniform screen produces no detectable structure, its RM is still preserved in any emission detected. Furthermore, the apparent RM of the cloud is *half* its true RM.

#### 4.2. Diffuse Polarized Emission

Figs 3 and 4 dramatically demonstrate the presence of large amounts of diffuse polarized emission throughout the SGPS Test Region. Comparing Figs 1 and 3, it is clear that much of this linearly polarized emission has no counterpart in total intensity. This can be understood in terms of the limited range of scales to which the interferometer is sensitive. The largest scale which the telescope can detect is usually determined by the shortest antenna spacing. In this case that spacing is 31 m, which corresponds to a spatial scale on the sky of  $\sim 25'$ . However, the mosaicing process allows us to recover information on larger scales (Cornwell 1988; Sault, Staveley-Smith, & Brouw 1996), in this case up to  $\sim 35'$ . Thus if there is diffuse polarized emission in the Test Region such that its total intensity is smoothly distributed, but the position angles of polarization vary on scales  $< 35'$ , then  $Q$  and  $U$  will contain structure small enough to be detected, but the emission in Stokes  $I$  will not be seen. This phenomenon is a common occurrence, and is seen whenever an interferometer surveys significant areas of the sky in polarization (Wieringa et al. 1993; Duncan et al. 1998; Gray et al. 1999; Haverkorn, Katgert, & de Bruyn 2000).

##### 4.2.1. Origin of the Polarized Emission

There are two possible mechanisms which can produce structure in polarized intensity when the total intensity is smooth. The first possibility is that considered in Section 4.1 above, in which the intrinsic polarized intensity is smooth, but for which compact foreground structure induces Faraday rotation on small scales. This will then produce structure in  $Q$  and  $U$  on smaller scales to which the interferometer is sensitive (see detailed discussion by Wieringa et al. 1993). If this is occurring, we expect to see no correlation between polarized and total intensity, since all the structure in polarization is generated by Faraday rotation alone. We also expect to see little correlation between structures observed at widely-separated observing frequencies, since the amount of Faraday rotation (and hence the level of structure produced by the foreground screen) is strongly frequency-dependent.

The second possibility is that the diffuse synchrotron emission has intrinsic structure in polarization, produced by a non-uniform magnetic field in the emitting regions. The brightest polarized structures in the single-dish 2.4 GHz polarization survey of Duncan et al. (1997a) are correlated with features in total intensity and have position angles across them which are particularly uniform, leading those authors to argue that this polarization corresponds to intrinsic structure in the emitting regions.

For the data presented here, a strong case can be made that both of the effects just discussed are contributing to the observed polarization. Since effects resulting from Faraday rotation are strongly dependent both on frequency and angular resolution (e.g. Burn 1966; Tribble 1991), the fact that most of the bright extended regions of polarization seen at 2.4 GHz are also seen at 1.4 GHz argues strongly that these structures must be intrinsic to the source of emission (as claimed by Duncan et al. [1997a] from the 2.4 GHz data alone). In the particular case of the bright polarized emission seen in Fig 6 in the range  $327^\circ < l < 331^\circ$ , Duncan et al. (1997a) suggest a possible association with the large SNR G325+0, the limbs of which can also faintly be seen in total intensity in 2.4 GHz data (Duncan et al. 1997b).

The one exception to the 1.4/2.4 GHz correspondence between regions of bright polarization is the ‘‘spur’’ of polarization seen near  $(329^\circ, +3^\circ)$ , which is also thought to be part of SNR G325+0 (Duncan et al. 1997b), but for which emission seems anti-correlated between 1.4 GHz and 2.4 GHz. This can be understood if internal depolarization is occurring at 1.4 GHz, in which polarized emission from different depths within the source undergoes differing amounts of Faraday rotation, and destructively interferes to produce reduced levels of overall polarization. We define the ‘‘depolarization factor’’,  $p_i$ , to be the ratio of detected to intrinsic intensity of linear polarization after internal depolarization. In the simplest models for internal depolarization (Burn 1966; Sokoloff et al. 1998), we find that:

$$p_i = \left| \frac{\sin R\lambda^2}{R\lambda^2} \right| \quad (3)$$

where  $R$  is the rotation measure through the entire source. It can be seen from Equation (3) that the observed polarization properties of this spur ( $p_i \sim 0$  at 1.4 GHz, but  $p_i \sim 1$  at 2.4 GHz) can be accounted for if the internal RM within the spur is of magnitude  $|R| \sim 70 \text{ rad m}^{-2}$ , a reasonable value if the spur is indeed part of a SNR (e.g. Moffett & Reynolds 1994a; Dickel & Milne 1998).

If we now consider regions of fainter polarized emission, we find that the location of and structure within such regions is poorly correlated between 1.4 and 2.4 GHz. This cannot easily be explained if this structure is intrinsic to the source of emission, but is exactly as would be expected if it is primarily produced by Faraday rotation in a foreground screen. There is generally more structure seen at 1.4 GHz than at 2.4 GHz, a result which we expect to be due to three separate effects. First, the angle through which a foreground screen will rotate polarized light is  $\sim 3$  times smaller at 2.4 GHz than at 1.4 GHz, so we expect to see much less patchy structure induced by the screen when viewed at the higher frequency. Second, if the position angle of polarization varies on scales which are resolvable at 1.4 GHz but not by the lower-resolution 2.4 GHz data, this can cause beam-depolarization at the higher frequency (see discussion in Section 4.3.1 below). Finally, if there are high RMs along the line-of-sight, this can then cause significant

bandwidth depolarization (see Equation [4] below) at 2.4 GHz (where  $1000 \text{ rad m}^{-2}$  causes  $\sim 100^\circ$  of rotation across the 145 MHz observing bandwidth) but not at 1.4 GHz (where the same RM produces  $\sim 30^\circ$  across each 8 MHz spectral channel).

By comparison with the 2.4 GHz data, we have argued above that structure in 1.4-GHz linear polarization which is intrinsic to the emitting regions is generally brighter than that produced by foreground Faraday rotation. In this case, we can then constrain the excess RMs which produce the latter structures. From Equation (A7), the intensity of polarized emission produced via foreground Faraday rotation is  $P = 2P_0 \sin(R_c \lambda^2)$ , where  $P_0$  is the intensity of the background polarization and  $R_c$  is the RM of the foreground material. If we set  $P < P_0$ , we find that  $|R_c| < 10 \text{ rad m}^{-2}$  to produce the observed structure, of which we will only detect a contribution of magnitude  $|R_c/2|$  (from Equation [A7]). Excess RMs of this magnitude are too small to be discerned from our data, and we thus do not expect to see enhanced RMs in regions where Faraday-induced polarization is occurring. Indeed, examination of Fig 7 shows no noticeable enhancements in RM in any particular regions, except around the edges of voids. We note that in the most clear-cut case of Faraday-induced polarization structure (Wieringa et al. 1993), the excess RMs measured were indeed of magnitude  $\sim 5 \text{ rad m}^{-2}$ , just as predicted here.

#### 4.2.2. Distance to the Polarized Emission

We have just shown that the contribution to the RM from discrete foreground clouds cannot be more than  $\sim 5 \text{ rad m}^{-2}$ . Thus the RMs seen in Fig 7 must be due almost entirely to Faraday rotation in the diffuse ISM between the source and the observer (i.e. the term  $R_s$  in Appendix A). We can estimate the distance from us at which the polarized emission is being produced by comparing the RMs for this diffuse emission to those measured for pulsars in the same part of the sky. If we only consider pulsars in the area  $320^\circ < l < 340^\circ$  and  $|b| < 3^\circ$ , we find ten measurements of pulsar RMs in the catalogue of Taylor et al. (1995), plus an additional eight more recent measurements listed by Han, Manchester & Qiao (1999). Using distances for these pulsars as determined from their dispersion measures (Taylor & Cordes 1993), we find that the only pulsars in this sample for which  $-100 \text{ rad m}^{-2} < \text{RM} < 0 \text{ rad m}^{-2}$  are the six sources whose distances lie in the range 1.3–4.5 kpc; pulsars at smaller distances have  $\text{RM} > 0 \text{ rad m}^{-2}$ , while at larger distances we generally find that  $|\text{RM}| > 100 \text{ rad m}^{-2}$ . Thus the distribution of RMs which we have measured argues for a distance to the emitting region in the range 1.3–4.5 kpc, corresponding to pulsars with RMs which are similarly small and negative. Independent measurements further limit the distance to the source of polarized emission: a lower limit of 2 kpc has been inferred from H I absorption towards polarized emission in this same region of the sky (Dickey 1997), while in Section 4.4.3 below we argue from the depolarizing effect of H II regions that this emission must be produced between 3 and 6.5 kpc. Taking into account all these constraints, we find that all observations are consistent with polarized emission in the Test Region originating at a mean distance  $3.5 \pm 1.0 \text{ kpc}$ .

Considering the spiral structure of the Galaxy in this direction (e.g. Georgelin & Georgelin 1976; Caswell & Haynes 1987), we find that the line-of-sight is crossed by three spiral arms: the Carina arm at a distance of  $\sim 1.5 \text{ kpc}$ , the Crux arm at  $\sim 3.5 \text{ kpc}$ , and the Norma arm, which runs nearly parallel to the line-of-sight in the range 6.5–10.5 kpc. Given that the diffuse component of synchrotron emission from the Galaxy originates

primarily in its spiral arms (Beuerman, Kanbach, & Berkhuisen 1985), it thus seems reasonable to conclude from our distance estimate that the polarization we are detecting originates predominantly in the Crux arm at 3.5 kpc.

It is not surprising that we do not detect polarization from the more distant Norma arm, because this structure is largely tangent to our line-of-sight. Internal Faraday rotation within this arm will thus be significant, largely depolarizing the emission from it (Burn 1966; Sokoloff et al. 1998). However, no such effects apply to the nearer Carina arm. We can limit the amount of polarization coming from this arm by considering polarized emission in the direction of the H II region RCW 94, which, at a distance of 3 kpc (Caswell & Haynes 1987), is behind the Carina arm. As shown in Figs 10 and 11, and discussed in Section 4.4.1 below, a halo surrounds RCW 94, through which background emission is completely depolarized. The lack of foreground polarization in this halo limits the relative contribution of polarization being produced in the Carina arm to  $\lesssim 20\%$  of that coming from the Crux arm. Because the Carina arm is at less than half the distance of the Crux arm, comparable polarized structures generated in it will have a correspondingly larger angular size, and may thus go largely undetected by the interferometer.

#### 4.2.3. Canals of Low Polarization

The polarization seen at 1.4 GHz is riddled with narrow canals of reduced polarization, running randomly through it. Such structures have been seen in various other wide-field images of radio polarization, most notably in the data of Duncan et al. (1996), Uyaniker et al. (1999) and Haverkorn et al. (2000). Haverkorn et al. (2000) specifically consider these canals, and show that in their data, the polarization position angles on either sides of these canals always differ by  $90^\circ$ . This demonstrates that these canals are produced by beam depolarization, in which perpendicular position angles are averaged together over a resolution element to result in no net polarization. Haverkorn et al. (2000) interpret these canals as being due to changes in the foreground RM by just the amount to produce a  $90^\circ$  rotation in position angles.

It is beyond the scope of this paper to make a detailed analysis of the properties of these canals as was carried out by Haverkorn et al. (2000). However, it can be seen in Fig 5 that there is a sudden change in position angle around the boundary of each patch of polarization — most of these sudden changes indeed correspond to canals. Furthermore, examination of specific regions indicates that most of the canals we see are one beamwidth wide, and that at the positions of almost all of these canals, a sudden change in position angle by  $\sim 90^\circ$  is seen. We demonstrate this in Fig 12, where we show the polarized intensities and polarized position angles in a region near  $(331.5^\circ, +3.0^\circ)$  containing several canals. Thus our observations support the conclusion of Haverkorn et al. (2000), that canals occur due to beam depolarization over adjacent regions of differing position angle.

However, when one examines the change in RM across these canals, we find that in general the RM does not noticeably change, and certainly does not shift by the  $33 \text{ rad m}^{-2}$  required to rotate the position angle of polarization by  $90^\circ$  at 1.4 GHz. This is apparent in Fig 12, where it can be seen that changes in RM across a canal are no more significant than changes in RM seen within each bright clump of polarized emission. The canals we see are thus possibly intrinsic to the source of polarized emission, and represent emitting regions where the mag-

netic field geometry is significantly non-uniform. These canals are not seen in the 2.4 GHz data shown in Fig 6, presumably because of the much poorer angular resolution of these data.

#### 4.3. Voids in Polarization

Figs 3 and 4 demonstrate the presence of two voids of polarization in the Test Region, each a few square degrees in extent. These voids have the following properties:

- They are approximately elliptical in shape.
- They have no counterparts in total intensity.
- The polarized intensity falls steadily to zero as one considers lines of sight projected increasingly close to their centers. This is demonstrated for void 1 in Fig 13, where we plot the mean polarized intensity in the range  $330^\circ 0 < l < 332^\circ 2$ , averaged between  $b = 0^\circ 7$  and  $b = 1^\circ 2$ . This region is marked by a box in Fig 4. In the interior of these voids, there is no detectable polarization down to a limit  $L \lesssim 1.5$  mJy beam<sup>-1</sup>, a factor 3–4 less than seen immediately outside the voids.
- The voids are also seen at 2.4 GHz. At this higher frequency, the intensity of polarization decreases by a factor of  $\sim 2$ –3 in their interiors relative to nearby regions of bright polarization.
- As one moves from the edges of the voids into their interiors, the polarized intensity becomes progressively fainter and clumpier.
- Large rotation measures ( $|RM| > 150$  rad m<sup>-2</sup>) are seen around the edges of these voids.

To the best of our knowledge, voids in polarization such as those described here have not been previously reported. Gray et al. (1999) detected large regions of depolarization in a polarimetric survey of the 2nd Galactic quadrant, carried out at the same frequency and spatial resolution as for the SGPS. However the voids which Gray et al. (1999) describe are coincident with, and have a morphology which is strongly correlated with, the bright H II regions W3 and W4. The voids in the SGPS, on the other hand, have no such counterparts detected in total intensity. Meanwhile, Duncan et al. (1999) have recently presented a survey of 2.7 GHz polarization in the 1st Galactic quadrant, using the 100-m Effelsberg radiotelescope. They find in their data that regions of low linear polarization coincide with regions of enhanced H I emission, and propose that these H I clouds are depolarizing emission propagating through them. However, we have examined the SGPS H I data for this region (McClure-Griffiths et al. 2000d), and find no structures or enhancements in H I coincident with the voids.

We thus conclude that the voids seen in the SGPS Test Region represent a previously unidentified phenomenon. There are two possible explanations to account for them: either they represent regions where the level of intrinsic polarization is low, or they are the result of propagation through a foreground object, whose properties have depolarized the emission at both 1.4 and 2.4 GHz.

We think the former possibility to be unlikely for two reasons. Firstly, if the voids are intrinsic to the emitting regions, then the distance of 3.5 kpc inferred in Section 4.2.2 implies that they are hundreds of parsecs across — it is hard to see what

could produce such uniformly low polarized intensity across such large regions. Secondly, for structure intrinsic to the emitting regions, we expect that the morphology of polarization will either be correlated or anti-correlated with structure seen in total intensity (the latter if the voids are the result of internal depolarization), as discussed in Section 4.2.1 above. However, Fig 2 demonstrates that the appearance of the total intensity emission within the voids is no different from elsewhere in the field. We therefore conclude that the voids cannot easily be explained as being intrinsic to the emitting regions.

In further discussion, we consider in more detail the second possibility, that the voids are caused by foreground depolarization. There are several mechanisms through which such an effect can occur (see Burn 1966; Tribble 1991; Sokoloff et al. 1998). The first of these is bandwidth depolarization, which occurs when there is significant Faraday rotation across a single spectral channel. This causes polarization vectors at either edge of the channel to be out of phase, and hence the polarized fraction to be reduced when averaged across the channel. The degree of bandwidth depolarization is given by (e.g. Gardner & Whiteoak 1966):

$$p_b = \left| \frac{\sin \Delta\Theta}{\Delta\Theta} \right| \quad (4)$$

where  $p_b$  is the depolarization factor as defined in Section 4.2.1 above but due to bandwidth effects, and  $\Delta\Theta = 2RMc^2\Delta\nu/\nu^3$  is the change in angle across a spectral channel of width  $\Delta\nu$ . An important constraint on bandwidth depolarization comes from source 21 in Table 1, which is significantly linearly polarized despite being deep within void 1. The RM measured for this source is  $-762 \pm 12$  rad m<sup>-2</sup>, and it can be seen in Fig 9 that the fit to the data is very good ( $\chi_r^2 = 1.2$ ). It is highly likely that the value measured is the true RM for this source: if there were additional turns of Faraday rotation between each spectral channel, this would require  $|RM| > 5000$  rad m<sup>-2</sup>, which from Equation (4) corresponds to a bandwidth-depolarization factor  $p_b \approx 0.15$ . This would then imply that the intrinsic fractional polarization of this source is  $\sim 45\%$ , significantly greater than for any other source in the Test Region or for extragalactic sources in general. We thus regard it highly likely that there are no ambiguities in the RM which we have measured.

The measured RM of  $-762$  rad m<sup>-2</sup> then differs by no more than  $\sim 1000$  rad m<sup>-2</sup> from the RM value predicted through the Galaxy at this position by Dickey et al. (in preparation). This difference is an upper limit on the total Faraday depth of void 1 at this position. We can thus immediately rule out bandwidth depolarization as an explanation for the voids, as a RM of  $\pm 1000$  rad m<sup>-2</sup> produces negligible bandwidth depolarization in our data ( $p_b \sim 0.95$ ), and could not produce the voids which we see.

A second cause of depolarization is a spatial gradient in RM. Such a gradient will produce a variation in the angle of polarization as a function of position. If this variation is significant when averaged across a single synthesized beam, the polarized fraction can be greatly reduced. Provided the RM gradient is resolved, the amount of depolarization produced within a Gaussian synthesized beam is given by (Sokoloff et al. 1998):

$$p_g = e^{-\frac{1}{\log_e 2} \left( \frac{dRM}{dr} \right)^2 \lambda^4} \quad (5)$$

where  $\frac{dRM}{dr}$  is the gradient of the RM across the sky in units of rad m<sup>-2</sup> beam<sup>-1</sup>, and  $p_g$  is the depolarization factor due to gradient effects. While only mild spatial gradients in RM, of

the order of  $\sim 25 \text{ rad m}^{-2} \text{ beam}^{-1}$ , are required to cause significant depolarization at 1.4 GHz, for any reasonable geometry these gradients in RM will be most significant near the edges of the structure (see discussion on RM gradients in Section 4.4.1 below). Fig 13 clearly demonstrates that in fact depolarization is mildest near the edges of the voids, and becomes severe in the interior. Thus it is difficult to see how gradients in RM can account for the voids.

The remaining possibility is that depolarization in the voids is due to beam depolarization, in which the RM varies randomly on small scales. Depolarization occurs when linearly polarized emission Faraday rotated with many different RMs (and hence different position angles) is averaged over the beam. Beam depolarization has the specific property that it will depolarize extended emission, but does not affect the polarized intensity of point sources. This can thus account for the presence of the polarized source 21 within void 1. Furthermore, a characteristic property of mild beam depolarization is that it induces a cell-like structure in the distribution of polarized intensity (e.g. Moffett & Reynolds 1994a,b), just as is seen around the perimeters of the voids.

In the following discussion, we show that the properties of void 1 can be understood using a simple model of beam depolarization. (We do not consider void 2 in detail because its perimeter is less well-defined, but similar arguments apply.)

#### 4.3.1. A Model for Void 1

We consider void 1 to be caused by a sphere of uniform electron density  $n_e \text{ cm}^{-3}$ , centered on  $(332.5, +1.2)$  with a radius of  $1.4$ . If the distance to the sphere is  $d$  kpc, this corresponds to a spatial diameter  $2R = 49d$  pc. The resolution of the observations is  $\sim 1$  arcmin, corresponding to a spatial resolution  $\delta = 0.3d$  pc.

Within the sphere, we suppose there are both random and ordered components to the magnetic field. The ordered component is uniform, and has mean value  $B_u \mu\text{G}$ , oriented at an angle  $\theta$  to the line of sight. The random component has magnitude  $B_r \mu\text{G}$ : we assume that the random component is coherent within individual cells of size  $l$  pc, but that the orientation from cell to cell is random. Uniformly polarized rays which propagate through a different series of cells will experience differing levels of Faraday rotation, resulting in beam depolarization when averaged over many different paths.

The level of depolarization resulting from this process depends on two factors: the dispersion of RMs produced by passage through the sphere,  $\sigma_{\text{RM}} \text{ rad m}^{-2}$ , and the characteristic scale on which these fluctuations occur,  $\psi$  arcsec.

We first assume that the cells in the source are arranged in a regular grid, so that two adjacent rays either pass through the same sequence of cells, or through completely independent sequences. In this case the scale for RM fluctuations is equal to the cell size, so that  $\psi = 200l/d$  arcsec. We can relate  $\sigma_{\text{RM}}$  to the properties of an individual cell as follows. Consider radiation passing through a single cell within the source. The rotation measure produced by passage through this cell is given by:

$$\text{RM}_i = Kn_e l (B_r \cos \phi_i + B_u \cos \theta), \quad (6)$$

where  $\phi_i$  is the angle to the line of sight of the random component of the field within that cell. The total RM after passage

through  $N$  cells is then:

$$\text{RM} = \sum_{i=1}^N \text{RM}_i = Kn_e l \left( NB_u \cos \theta + B_r \sum_{i=1}^N \cos \phi_i \right) \text{ rad m}^{-2}. \quad (7)$$

The  $N$  values of  $\cos \phi_i$  are independently distributed with a mean of 0 and a variance of  $1/3$ . Then using the central limit theorem, we find that for large  $N$ ,  $\sum_{i=1}^N \cos \phi_i$  is normally distributed with mean 0 and variance  $N/3$ . Thus we expect:

$$\langle \text{RM} \rangle = Kn_e DB_u \cos \theta \text{ rad m}^{-2} \quad (8)$$

and

$$\sigma_{\text{RM}} = Kn_e \frac{B_r}{\sqrt{3}} \sqrt{Dl} \text{ rad m}^{-2}, \quad (9)$$

where  $D = Nl$  pc is the depth through the source at a particular position.

The above result assumes that adjacent patches of different RM correspond to completely independent paths through the source. However, it is more realistic to assume that the cells do not fall in ordered columns, but that each layer of cells is randomly aligned with respect to every other layer. In this case, the values of RM in adjacent patches are correlated, since two neighboring paths will have some cells in common, and we thus expect a smaller value of  $\sigma_{\text{RM}}$  than in the case of an ordered grid of cells. Furthermore, we expect the scale of RM fluctuations to be smaller, since one no longer needs to move a full cell across the source before encountering a region of differing RM.

We have carried out Monte Carlo simulations to quantify how  $\psi$  and  $\sigma_{\text{RM}}$  change in the case of randomly aligned cells. We find that the characteristic scale of RM fluctuations is decreased by a factor of two, corresponding to an angular scale half the cell size, so that  $\psi = 100l/d$  arcsec. Furthermore, we find that the RMs are still normally distributed, but with a dispersion smaller by a factor of 2, so that

$$\sigma_{\text{RM}} = Kn_e \frac{B_r}{2\sqrt{3}} \sqrt{Dl} \text{ rad m}^{-2}. \quad (10)$$

For particular values of  $\psi$  and  $\sigma_{\text{RM}}$ , Tribble (1991) has shown that the resulting depolarization factor due to beam depolarization is:

$$p_f^2 \approx \frac{1 - e^{(-\kappa^2 - 4\sigma_{\text{RM}}^2 \lambda^4)}}{1 + 4\sigma_{\text{RM}}^2 \lambda^4 / \kappa^2} + e^{(-\kappa^2 - 4\sigma_{\text{RM}}^2 \lambda^4)} \quad (11)$$

where  $\kappa = 5.72 \times 10^{-3} \psi d / \delta$ . For increasingly smaller scales for the RM fluctuations (i.e. smaller values of  $\kappa$  and  $\psi$ ), depolarization becomes increasingly severe (i.e.  $p_f$  decreases). In the limiting case that  $\kappa \rightarrow 0$ , this expression reduces to (Burn 1966; Tribble 1991):

$$p_f = e^{-2\sigma_{\text{RM}}^2 \lambda^4}. \quad (12)$$

For a spherical geometry we have that  $D = 2\sqrt{R^2 - r^2}$  pc, where  $r$  pc is the impact parameter of the line of sight relative to the center of void 1. We can then adopt a particular value of  $\psi$  and then use Equations (10) and (11) to fit to the profile of polarized intensity seen in Fig 13.

However an important constraint on any model is that significant beam depolarization is also seen within void 1 at 2.4 GHz. At the much poorer resolution of the 2.4 GHz data (10.4 arcmin), we can use Equation (12) to predict the degree of depolarization seen at 2.4 GHz. The depolarization seen at 2.4 GHz



within void 1 has value  $p_f \sim 0.3 - 0.5$ , implying peak dispersions in the RM fluctuations of  $\sigma_{\text{RM}} \sim 35 - 50 \text{ rad m}^{-2}$ .

Given this constraint, we find that the only parameters which can reasonably fit the 1.4 GHz polarization profile seen in Fig 13, while simultaneously producing the appropriate levels of depolarization at 2.4 GHz, are  $\psi \approx 60'' - 80''$  (i.e.  $l \approx [0.6 - 0.7]d$  pc and  $\kappa \approx 1.1 - 1.5$ ) and  $n_e B_r \approx 30/d \mu\text{G cm}^{-3}$ . The 1.4 GHz polarized intensity predicted by this model is plotted in Fig 13. Shifting the assumed center and radius of the sphere by reasonable amounts changes these parameters by less than 10%. We know that  $d < 3.5$  kpc (since this is the distance to the polarized emission behind the void). Thus a joint lower bound on the density and random component of the field within the sphere is  $n_e B_r \gtrsim 9 \mu\text{G cm}^{-3}$ .

We can limit the electron density in the sphere by noting that the 2.4 GHz surface brightness in this direction in the survey of Duncan et al. (1995) is  $\sim 4$  K. This is then an upper limit on the brightness temperature of any free-free emission produced by the sphere. For optically thin emission, and assuming a typical electron temperature  $T_e = 8000$  K, an upper limit on the emission measure through the center of the sphere (e.g. Mezger & Henderson 1967) is then  $\text{EM} = \int n_e^2 dl < 7000 \text{ pc cm}^{-6}$ . This limit implies that  $n_e < 12d^{-0.5} \text{ cm}^{-3}$ , which together with the fit to the polarization profile described above implies  $B_r > 2.5d^{-0.5} \mu\text{G} \gtrsim 1.3 \mu\text{G}$ .

We can constrain the strength of the ordered component of the field by noting that near the edges of the voids, where gradients in RM are most severe, depolarization due to such gradients is negligible. Specifically, the behavior of polarized intensity in Fig 13 is such that we can approximate  $p_g > 0.5$  at  $r = R - \delta$ . Using the fact that the gradient in RM is given by:

$$\frac{d\text{RM}}{dr} = \frac{-2Kn_e B_u r \delta \cos \theta}{\sqrt{R^2 - r^2}}, \quad (13)$$

we can use Equations (5) and (8) to determine that  $n_e B_u \cos \theta \lesssim 4.9/d \mu\text{G cm}^{-3}$ . The peak RM through the void is then  $\lesssim 200 \text{ rad m}^{-2}$ , consistent with the limit  $|\text{RM}| < 1000 \text{ rad m}^{-2}$  inferred from the total RM of source 21 as discussed in Section 4.3 above.

If we assume that the strengths of the uniform and the random components of the field are approximately equal (e.g. Jones 1989; Goodman & Heiles 1994), then our combined limits on  $B_u$  and  $B_r$  imply that  $\cos \theta \lesssim 0.15$ , so that  $B_u$  is largely in the plane of the sky.

#### 4.3.2. Interpretation of the Model

While the above model is simplistic in its assumptions, it successfully reproduces the polarization profile at 1.4 GHz, accounts for depolarization seen also at 2.4 GHz, and explains the fact that source 21 is not depolarized nor has an excessive RM.

While voids in polarization such as described here have not been previously reported, localized regions of similarly enhanced RM fluctuations have been seen in polarization studies of extragalactic sources. In particular, Simonetti & Cordes (1986) saw fluctuations in RM on arcmin scales at the level of  $\sigma_{\text{RM}} \lesssim 5 \text{ rad m}^{-2}$  over most of the sky, but found enhanced fluctuations of magnitude  $\sigma_{\text{RM}} \approx 40 \text{ rad m}^{-2}$  in a region of the Galactic Plane near  $l = 90^\circ$ . Similarly, Lazio, Spangler & Cordes (1990) measured the RMs of sources behind the Cygnus OB1 association, and found RM fluctuations on arcmin scales at the level of  $\sigma_{\text{RM}} \sim 25 \text{ rad m}^{-2}$ .

It has been suggested that the high dispersion in RM in such regions is the result of either an expanding wind bubble or supernova blast wave, either of which will sweep a dense shell of material from its environment. Propagation through the turbulence and instabilities produced in this surrounding shell will then generate the observed fluctuations in RM (Simonetti & Cordes 1986; Spangler & Cordes 1998). However, because the severity of beam depolarization increases with the line-of-sight pathlength through a source, the polarization profile seen in Fig 13 cannot be easily produced by a thin shell, for which we would expect to see significantly more beam depolarization around the perimeter than through the center. Furthermore, one might expect to see the swept up material in H I, and yet examination of the SGPS H I data for this region shows no such features in this region.

We therefore argue that the voids we observe are best explained as structures which are turbulent throughout their extent, rather than in a shell around their perimeters. We propose that the voids are caused by low density H II regions, which have extents, densities and magnetic fields similar to those inferred here (e.g. Heiles & Chu 1980; Lockman, Pisano, & Howard 1996; Vallée 1997). This interpretation is supported by the presence of significant levels of diffuse H $\alpha$  emission coincident with void 2 (Amram et al. 1991; Georgelin et al. 1994). There are multiple overlapping H $\alpha$  complexes in this low-latitude region, so it is not possible to uniquely identify an H II region which might be specifically associated with void 2. However, we note that most of the H $\alpha$  nebulae in this region are at distances of between 1 and 3 kpc (Georgelin et al. 1994), placing them in front of the polarized background as required in our model.

Unfortunately, no information on H $\alpha$  is currently available for void 1. We can estimate an approximate distance to this region by noting that turbulence in H II regions is consistently seen to have an outer scale of  $\sim 0.15$  pc (Miville-Deschênes, Joncas, & Durand 1995; Joncas 1999). Requiring this to be comparable to the scales inferred for turbulent cells in void 1, we can infer an approximate distance to void 1 of  $d \sim 0.25$  kpc.

It is interesting to note that the O9V star HD 144695, at  $(332^\circ 25', +1^\circ 30')$ , is very close to the projected center of void 1, and is at a distance of  $0.30 \pm 0.16$  kpc (Garmany, Conti, & Chiosi 1982; Perryman et al. 1997). If we suppose that void 1 is a Strömgren sphere associated with this star, its radius of  $7.3 \pm 3.9$  pc implies a density  $n_e \sim 25 \pm 20 \text{ cm}^{-3}$  (Prentice & ter Haar 1969), which is consistent with the limit  $n_e < 12d^{-0.5} \sim 20 \text{ cm}^{-3}$  inferred above from the upper limit on emission measure.

Two properties of the voids which our simple model cannot account for are the requirement that the uniform component of the magnetic field be largely oriented in the plane of the sky, but that we generally observe coherent regions of large RM (of the order of a few hundred  $\text{rad m}^{-2}$ ) around the edges of the voids. We suggest that both these results can be explained if the uniform component of the magnetic field within the void is oriented so that its radial component (relative to the center of the void) is always zero. This will result in a magnetic field perpendicular to the line of sight over most of the void, but which is parallel to the line of sight (and can thus potentially produce high RMs) around the perimeter. If the ambient magnetic field is well-ordered, such a field geometry will naturally arise during the expansion phase of an H II region as it interacts with surrounding material. The amount of material swept up by this process would be much smaller than in the case of

a rapidly expanding wind bubble or SNR, consistent with the lack of detection of an H I shell surrounding the void.

To summarize, the properties of void 1 can be explained if it is an H II region of density  $n_e \sim 20 \text{ cm}^{-3}$  and magnetic field  $B_r \approx B_u \sim 5 \text{ } \mu\text{G}$  at a distance  $d \sim 0.3 \text{ pc}$ , potentially associated with the O9V star HD 144695. The depolarization which we observe is caused by turbulence on scales  $\sim 0.2 \text{ pc}$ , with dispersion in RM  $\sigma_{\text{RM}} = 35 - 50 \text{ rad m}^{-2}$ .

Considerable further study will be required before we are able to properly ascertain the nature of the voids. In the particular case of void 1, H $\alpha$  observations are highly desirable, both to better constrain the emission measure through the source and to determine a kinematic distance for it from the velocity of the line emission. More generally, it is likely that the full SGPS will allow us to identify a large number of such voids, which will allow us to better determine the properties of the population.

#### 4.4. H II regions

##### 4.4.1. Depolarization seen towards RCW 94

As seen in Figs 10 and 11, the H II region RCW 94 shows reduced linear polarization in its interior, and is furthermore surrounded by a halo in which no linear polarization is detected. We take these results to indicate that this source is depolarizing background emission propagating through it, as was seen towards the H II complex W3/W4 by Gray et al. (1999). We now attempt to account quantitatively for this behavior.

The region of depolarization seen towards RCW 94 extends beyond the boundaries of the source as seen in total intensity (indeed this is where depolarization is most extreme).<sup>10</sup> This indicates that the full extent of the H II region is larger than that part of it which produces detectable emission. In subsequent discussion, we assume the extent of the source to be a circle of radius 16 arcmin, corresponding to the extent of the depolarized region.

The various mechanisms by which a foreground source can depolarize emission propagating through it were discussed in Section 4.3. Since H II regions are not expected to be sources of polarization themselves, we can immediately rule out internal depolarization. In the following discussion, we assume some simple geometries for RCW 94, and see if the polarized intensity observed towards it can then be understood in terms of bandwidth, gradient and beam depolarization. The levels of depolarization which we are trying to account for are  $p \sim 0.5$  in regions coincident with bright radio continuum, and  $p \lesssim 0.2$  in a halo surrounding this region.

We first assume for RCW 94 the same geometry as for void 1 discussed above: a sphere of radius  $R \text{ pc}$  at distance  $d \text{ kpc}$  observed at a spatial resolution  $\delta \text{ pc}$ , within which the electron density has a uniform value of  $n_e \text{ cm}^{-3}$ . In this particular case, we have that  $d = 3 \text{ kpc}$ ,  $2R = 28 \text{ pc}$ ,  $\delta = 0.9 \text{ pc}$ , and  $n_e = 20 \text{ cm}^{-3}$  (Shaver et al. 1983; Caswell & Haynes 1987). As in Section 4.3.1 above, we assume a magnetic field with a uniform component  $B_u$ , inclined at an angle  $\theta$  to the line of sight, and with a random component  $B_r$ , characterized by a turbulent scale  $l$ .

To determine the total depolarization, we combine Equations (4), (5) and (11), so that:

$$p = p_b p_g p_f. \quad (14)$$

Because the 2.4 GHz data are of insufficient spatial resolution to

provide useful information on this region, we cannot uniquely constrain the parameters of the source as was done for void 1 in Section 4.3.1. However, a general feature of any set of parameters is that the terms in  $p_b$  and  $p_g$  increase (i.e. cause less depolarization) with increasing  $r$ , while  $p_g$  decreases with increasing  $r$ . An example of this behavior is shown in the upper panel of Fig 14, where we show the expected polarization profile for reasonable parameters  $B_r = B_u = 1.2 \text{ } \mu\text{G}$ ,  $l = 0.15 \text{ pc}$  and  $\theta = 60^\circ$ . In this case the peak RM through the source is  $270 \text{ rad m}^{-2}$ , so that bandwidth depolarization is negligible. Beam depolarization is most severe in the center, but becomes increasingly less significant at larger radii. Depolarization due to RM gradients is only significant in the outer half of the source, and completely depolarizes the emission beyond  $r/R \gtrsim 0.7$ . The net polarized intensity then qualitatively agrees with observations, in that it produces  $p \sim 0.5$  near the center of the source and  $p \lesssim 0.2$  around its edges.

However, this model is at odds with the shape of the observed polarization profile seen in Fig 11, which has approximately constant surface brightness at small radii, and suddenly decreases around the outer edges of the source. We can find no set of parameters for a spherical geometry which can reproduce this behavior. Note that if we relax the assumption that  $n_e$  and  $B_u$  are uniform, and rather model either parameter as decreasing with radius, then the gradients in RM are more severe, and  $p_f$  will fall to zero for values of  $r/R$  smaller than observed.

Thus in order to reproduce the observed behavior, we must abandon a spherical model, and instead consider a geometry in which the RM is approximately constant as a function of radius for  $r/R < 0.7$  (so that  $p_b$  and  $p_f$  are constant and  $p_g$  is unity), but which then decreases linearly to zero for  $0.7 < r/R < 1$  (so that  $p_g$  suddenly decreases to zero around the edges). A reasonable such geometry is a cylinder viewed face-on, in the interior of which  $n_e$  is constant, but around the edges of which  $n_e$  falls linearly to zero. Such a model produces a constant emission measure (EM) for  $r/R < 0.7$ , in agreement with the approximately constant surface brightness in H $\alpha$  seen in this region (Georgelin et al. 1994). The model also results in a low EM around the outer edges of the source, which can account for the fact that the size of the source as seen in depolarization is larger than that delineated by its radio continuum and H $\alpha$  emission.

When we model this geometry using the same parameters as in the spherical case above ( $n_e = 20 \text{ cm}^{-3}$ ,  $B_u = B_r = 1.2 \text{ } \mu\text{G}$ ,  $l = 0.15 \text{ pc}$  and  $\theta = 60^\circ$ ), and assuming that the depth through the source is equal to its diameter projected onto the sky, we obtain a predicted polarization profile as shown in the lower panel of Fig 14. This now correctly reproduces the observed polarization properties of the source.

##### 4.4.2. Interpretation of the Model

The fall-off in  $n_e$  which we have invoked to account for the depolarized halo around RCW 94 is suggestive of similar features seen in polarimetric observations of the H II regions W3, W4 and W5 (Gray et al. 1999). Not only do these sources depolarize the emission propagating through them in a similar way as seen through the interior of RCW 94, but there are also suggestions that the depolarization extends beyond the boundaries of these sources as defined by their continuum radio emission. Gray et al. (1999) interpret this to indicate that these H II regions are embedded in low density cocoons, the existence of

<sup>10</sup>This is also beyond the extent of the source as seen in H $\alpha$ , for which the size and shape are similar to those seen in the radio (Georgelin et al. 1994).

which has been previously inferred from recombination line emission seen both in the vicinity of specific H II regions and also along the entire Galactic Plane (Hart & Pedlar 1976; Anantharamaiah 1985; Azcárate, Cersosimo, & Colomb 1987).

However, the presence of significant CO emission at the same position and systemic velocity as for RCW 94 (Bronfman et al. 1989) suggests that the H II region may rather be interacting with a molecular cloud. This possibility is supported by H I observations of the region, which show that RCW 94 is embedded in a shell of H I emission, which is further surrounded by a ring of decreased H I emission (McClure-Griffiths et al. 2000a). McClure-Griffiths et al. (2000d) argue that this structure in H I confirms that RCW 94 is embedded in a molecular cloud, the shell of emission resulting from H<sub>2</sub> molecules dissociated by the H II region, and the surrounding region of reduced H I corresponding to regions of undisturbed molecular material. Simulations of H II regions evolving within molecular clouds (Rodríguez, Tenorio-Tagle, & Franco 1995 and references therein) show that for certain forms of the density profile within the parent cloud, the shock driven into the cloud by the embedded expanding H II region can produce a halo of partially ionized material around the latter's perimeter, which would produce the fall-off in  $n_e$  required to produce the depolarization observed in Figs 10 and 11.

We note that high RMs are seen around the perimeter of RCW 94 in Fig 7. This may be due to the ambient magnetic field “wrapping around” the expanding H II region as was proposed in Section 4.3.2 for the voids. Alternatively, these high RMs may simply be due to the magnetic fields and ionized material in which the entire RCW 94 complex (see e.g. Georgelin et al. 1994) is embedded.

#### 4.4.3. Limits on the distance to the polarized emission

The fact that RCW 94 (and possibly also G326.7+0.5) show this depolarizing effect implies that the diffuse background polarization must be propagating through these sources, and hence must be behind them. This puts a lower limit of  $\sim 3$  kpc on the distance to the source of the diffuse polarized emission in this direction.

Of the other  $\sim 30$  H II regions in the field, most are either in large voids of depolarization, or have sufficiently low densities and diameters that they are unlikely to produce significant depolarization. The one exception to this is the H II region G331.6–0.0, which seems to have no effect on polarization at its position, but which should produce significant depolarization.

G331.6–0.0 has  $n_e = 250 \text{ cm}^{-3}$  (Shaver et al. 1983) and is at a distance  $d = 6.5$  kpc (Caswell et al. 1975; Caswell & Haynes 1987), corresponding to a linear extent  $2R = 30$  pc. Given that magnetic field and density are generally correlated (Troland & Heiles 1986; Vallée 1997), it is unlikely that the magnetic field is any less than  $B \sim 1 \mu\text{G}$  as assumed for the lower density source RCW 94. We therefore expect significant ( $p < 0.1$ ) depolarization through the center of the source, due to both bandwidth and beam effects. In fact, we observe in this region that  $p \sim 1$ . The simplest interpretation of this discrepancy is that this source is behind the polarized emission seen at its position. This limits the distance of the polarization background to be closer than 6.5 kpc.

## 5. CONCLUSIONS

The ATCA's sensitivity, spatial resolution and spectral flexibility have allowed us to study linear polarization and Faraday

rotation in the SGPS Test Region in unprecedented detail. Even though this field covers less than 7% of the full survey, a variety of structures are apparent from this preliminary study.

We identify the following main features seen in polarization:

- Diffuse linear polarization seen throughout the Test Region, with structure on scales of degrees, and completely uncorrelated with emission seen in total intensity. The brightest polarized features most likely represent intrinsic structure in the source of emission, but fainter components are best explained as being imposed by Faraday rotation of a uniformly polarized background by foreground material. The rotation measures determined towards this emission generally lie between  $-100$  and  $0 \text{ rad m}^{-2}$ , which indicates that this emission originates at a distance of  $\sim 3.5$  kpc, most likely in the Crux spiral arm of the Galaxy.
- Two large regions devoid of polarization, each several degrees in extent, and with no counterparts in total intensity. We have considered one of these voids in detail, and have shown that the depolarization observed through it can be explained by turbulence within it on scales  $\sim 0.2$  pc. We find that the properties of the void are consistent with it being a nearby ( $\sim 250$  pc) H II region of density  $n_e \sim 20 \text{ cm}^{-3}$  and magnetic field  $B \sim 5 \mu\text{G}$ , possibly associated with the O star HD 144695.
- A halo of depolarization surrounding the H II region RCW 94. We interpret this as delineating a region of lower electron density surrounding the H II region. We propose that this region corresponds to a halo of ionized material resulting from the interaction of RCW 94 with a surrounding molecular cloud.

The results presented here demonstrate the value of interferometric polarimetry as a probe of the ISM. The full SGPS will allow us to accumulate many more examples of the types of features we have described here, with which we will be able to better determine their properties and distributions. Furthermore, we expect that the large-scale properties of polarized emission will be a function of position within the Galactic Plane (e.g. Duncan et al. 1997a, 1999), reflecting differing orientations of the spiral arms with respect to the line of sight. Overall, we anticipate that the SGPS will provide the opportunity for a comprehensive study of the magneto-ionic medium of the inner Galaxy, on scales ranging from sub-parsec turbulence up to the global structure of the spiral arms and disc.

We thank Veta Avedisova for supplying us with her extensive catalogue of star formation regions, and are grateful to Alyssa Goodman, Carl Heiles, Larry Rudnick and Ellen Zweibel for stimulating discussions on Faraday rotation, depolarization and turbulence. This research has made use of the NASA Astrophysics Data System and the CDS SIMBAD database. The Australia Telescope is funded by the Commonwealth of Australia for operation as a National Facility managed by CSIRO. This research has made use of NASA's Astrophysics Data System Abstract Service and of the SIMBAD database, operated at CDS, Strasbourg, France. B.M.G. acknowledges the support of NASA through Hubble Fellowship grant HST-HF-01107.01-A awarded by the Space Telescope Science Institute, which is operated by the Association of Universities for Research

in Astronomy, Inc., for NASA under contract NAS 5-26555. N.M.Mc-G. and J.M.D. acknowledge the support of NSF grant AST-9732695 to the University of Minnesota. N.M.Mc-G. is

supported by NASA Graduate Student Researchers Program (GSRP) Fellowship NGT 5-50250.

## REFERENCES

- Amram, P., Boulesteix, J., Georgelin, Y. M., Georgelin, Y. P., Laval, A., Le Coarer, E., Marcelin, M., & Rosado, M. 1991, *The ESO Messenger*, 64, 44.
- Anantharamaiah, K. R. 1985, *J. Astrophys. Astr.*, 6, 203.
- Avedisova, V. S. 1997, *Baltic Astronomy*, 6, 307.
- Azcárate, I. N., Cersosimo, J. C., & Colomb, F. R. 1987, *Rev. Mex. Astron. Astrofis.*, 15, 3.
- Beuerman, K., Kanbach, G., & Berkhuijsen, E. M. 1985, *A&A*, 153, 17.
- Bronfman, L., Alvarez, H., Cohen, R. S., & Thaddeus, P. 1989, *ApJS*, 71, 481.
- Burn, B. J. 1966, *MNRAS*, 133, 67.
- Caswell, J. L. & Haynes, R. F. 1987, *A&A*, 171, 261.
- Caswell, J. L., Murray, J. D., Roger, R. S., Cole, D. J., & Cooke, D. J. 1975, *A&A*, 45, 239.
- Clegg, A. W., Cordes, J. M., Simonetti, J. H., & Kulkarni, S. R. 1992, *ApJ*, 386, 143.
- Cooper, B. F. C. & Price, R. M. 1961, *Nature*, 195, 1084.
- Cornwell, T. J. 1988, *A&A*, 202, 316.
- Cornwell, T. J., Holdaway, M. A., & Uson, J. M. 1993, *A&A*, 271, 697.
- Dickel, J. R. & Milne, D. K. 1998, *AJ*, 115, 1057.
- Dickey, J. M. 1997, *ApJ*, 488, 258.
- Dickey, J. M., McClure-Griffiths, N., Gaensler, B., Green, A., Haynes, R. F., & Wieringa, M. H. 1999, in *New Perspectives on the Interstellar Medium*, ed. A. R. Taylor, T. L. Landecker, & G. Joncas, (San Francisco: Astronomical Society of the Pacific), 27.
- Duncan, A. R., Haynes, R. F., Jones, K. L., & Stewart, R. T. 1997a, *MNRAS*, 291, 279.
- Duncan, A. R., Haynes, R. F., Reich, W., Reich, P., & Gray, A. D. 1998, *MNRAS*, 299, 942.
- Duncan, A. R., Reich, P., Reich, W., & Fürst, E. 1999, *A&A*, 350, 447.
- Duncan, A. R., Stewart, R. T., Haynes, R. F., & Jones, K. L. 1995, *MNRAS*, 277, 36.
- Duncan, A. R., Stewart, R. T., Haynes, R. F., & Jones, K. L. 1996, *MNRAS*, 280, 252.
- Duncan, A. R., Stewart, R. T., Haynes, R. F., & Jones, K. L. 1997b, *MNRAS*, 287, 722.
- Ekers, R. D. & Rots, A. H. 1979, in *Image Formation from Coherence Functions in Astronomy*, ed. C. van Schooneveld, (Dordrecht: Reidel), p. 61.
- Faraday, M. 1844, *Experimental researches in electricity*, (London: R Taylor). Reprinted New York: Dover 1952.
- Frater, R. H., Brooks, J. W., & Whiteoak, J. B. 1992, *J. Electr. Electron. Eng. Aust.*, 12, 103.
- Gardner, F. F. & Whiteoak, J. B. 1966, *Ann. Rev. Astr. Ap.*, 4, 245.
- Garmany, C. D., Conti, P. S., & Chiosi, C. 1982, *ApJ*, 263, 777.
- Georgelin, Y. M., Amram, P., Georgelin, Y. P., le Coarer, E., & Marcelin, M. 1994, *A&AS*, 108, 513.
- Georgelin, Y. M. & Georgelin, Y. P. 1976, *A&A*, 49, 57.
- Goodman, A. A. & Heiles, C. 1994, *ApJ*, 424, 208.
- Gray, A. D., Landecker, T. L., Dewdney, P. E., & Taylor, A. R. 1998, *Nature*, 393, 660.
- Gray, A. D., Landecker, T. L., Dewdney, P. E., Taylor, A. R., Willis, A. G., & Normandeau, M. 1999, *ApJ*, 221.
- Green, A. J., Cram, L. E., Large, M. I., & Ye, T. 1999, *ApJS*, 122, 207. (<http://www.astrop.physics.usyd.edu.au/MGPS/>).
- Green, D. A. 2000, *A Catalogue of Galactic Supernova Remnants (2000 August Version)*, (Cambridge: Mullard Radio Astronomy Observatory). (<http://www.mrao.cam.ac.uk/surveys/snrs/>).
- Greisen, E. W. & Calabretta, M. 1995, in *Astronomical Data Analysis Software and Systems IV*, ed. R. A. Shaw, H. E. Payne, & J. J. E. Hayes, volume 77 of ASP Conference Series, (San Francisco: Astronomical Society of the Pacific), p. 233.
- Han, J. L., Manchester, R. N., & Qiao, G. J. 1999, *MNRAS*, 306, 371.
- Han, J. L., Manchester, R. N., Xu, R. X., & Qiao, G. J. 1998, *MNRAS*, 300, 373.
- Han, J. L. & Qiao, G. J. 1994, *A&A*, 288, 759.
- Hart, L. & Pedlar, A. 1976, *MNRAS*, 176, 547.
- Haverkorn, M., Katgert, P., & de Bruyn, A. G. 2000, *A&A*, 356, L13.
- Heiles, C. & Chu, Y.-H. 1980, *ApJ*, 235, L105.
- Joncas, G. 1999, in *Proceedings of the 2nd Guillermo Haro Conference*, ed. F. Franco & A. Carraminana, Cambridge University Press, 154.
- Jones, T. J. 1989, *ApJ*, 346, 728.
- Junkes, N., Fürst, E., & Reich, W. 1987, *A&AS*, 69, 451.
- Killeen, N. E. B., Bicknell, G. V., & Ekers, R. D. 1986, *ApJ*, 302, 306.
- Lazio, T. J., Spanger, S. R., & Cordes, J. M. 1990, *ApJ*, 363, 515.
- Lockman, F. J., Pisano, D. J., & Howard, G. J. 1996, *ApJ*, 472, 173.
- Matsui, Y., Long, K. S., Dickel, J. R., & Greisen, E. W. 1984, *ApJ*, 287, 295.
- McClure-Griffiths, N. M., Dickey, J. M., Gaensler, B. M., Green, A. J., Haynes, R. F., & Wieringa, M. H. 2000a, *Publ. Astron. Soc. Austral.*, . submitted.
- McClure-Griffiths, N. M., Dickey, J. M., Gaensler, B. M., Green, A. J., Haynes, R. F., & Wieringa, M. H. 2000b, *BAAS*, 195, 72.13.
- McClure-Griffiths, N. M., Dickey, J. M., Gaensler, B. M., Green, A. J., Haynes, R. F., & Wieringa, M. H. 2000c, *AJ*, 119, 2828.
- McClure-Griffiths, N. M., Green, A. J., Dickey, J. M., Gaensler, B. M., Green, A. J., Haynes, R. F., & Wieringa, M. H. 2000d, *ApJ*, . submitted.
- Mezger, P. G. & Henderson, P. 1967, *MNRAS*, 147, 471.
- Milne, D. K., Caswell, J. L., Kesteven, M. J., Haynes, R. F., & Roger, R. S. 1989, *Proc. Astr. Soc. Aust.*, 8, 187.
- Miville-Deschênes, M.-A., Joncas, G., & Durand, D. 1995, *ApJ*, 454, 316.
- Moffett, D. A. & Reynolds, S. P. 1994a, *ApJ*, 425, 668.
- Moffett, D. A. & Reynolds, S. P. 1994b, *ApJ*, 437, 705.
- Perryman, M. A. C. et al. 1997, *A&A*, 323, L49.
- Prentice, A. J. R. & ter Haar, D. 1969, *MNRAS*, 146, 423.
- Reynolds, J. E. 1994, *ATNF Technical Document Series*, 39.3040. ([http://www.narrabri.atnf.csiro.au/observing/users\\_guide/html/node215.html](http://www.narrabri.atnf.csiro.au/observing/users_guide/html/node215.html)).
- Rodríguez, J. A., Tenorio-Tagle, G., & Franco, J. 1995, *ApJ*, 451, 210.
- Sault, R. J., Bock, D. C.-J., & Duncan, A. R. 1999, *A&AS*, 139, 387.
- Sault, R. J., Hamaker, J. P., & Bregman, J. D. 1996, *A&AS*, 117, 149.
- Sault, R. J., & Killeen, N. E. B. 1999, *The Miriad User's Guide*, (Sydney: Australia Telescope National Facility). (<http://www.atnf.csiro.au/computing/software/miriad/>).
- Sault, R. J., Staveley-Smith, L., & Brouw, W. N. 1996, *A&AS*, 120, 375.
- Sault, R. J. & Wieringa, M. H. 1994, *A&AS*, 108, 585.
- Seeger, C. L. & Westerhout, G. 1961, *AJ*, 66, 294.
- Shaver, P. A., McGee, R. X., Newton, L. M., Danks, A. C., & Pottasch, S. R. 1983, *MNRAS*, 204, 53.
- Simard-Normandin, M. & Kronberg, P. P. 1980, *ApJ*, 242, 74.
- Simonetti, J. H. & Cordes, J. M. 1986, *apj*, 310, 160.
- Sokoloff, D. D., Bykov, A. A., Shukurov, A., Berkhuijsen, E. M., Beck, R., & Poezd, A. D. 1998, *MNRAS*, 299, 189.
- Spangler, S. R. & Cordes, J. M. 1998, *ApJ*, 505, 766.
- Spoelstra, T. A. T. 1984, *A&A*, 135, 238.
- Taylor, J. H. & Cordes, J. M. 1993, *ApJ*, 411, 674.
- Taylor, J. H., Manchester, R. N., Lyne, A. G., & Camilo, F. 1995, Unpublished (available at <ftp://pulsar.princeton.edu/pub/catalog>).
- Tribble, P. C. 1991, *MNRAS*, 250, 726.
- Troland, T. H. & Heiles, C. 1986, *ApJ*, 301, 339.
- Uyaniker, B., Fürst, E., Reich, W., Reich, P., & Wielebinski, R. 1999, *A&AS*, 138, 31.
- Vallée, J. P. 1997, *Fundamentals of Cosmic Physics*, 19, 1.
- Wieringa, M. H., de Bruyn, A. G., Jansen, D., Brouw, W. N., & Katgert, P. 1993, *A&A*, 268, 215.

TABLE 1  
 COMPACT SOURCES SHOWING LINEAR POLARIZATION.

Source No. (1)	l (2)	b (3)	$L$ (mJy) (4)	$I$ (mJy) (5)	$L/I$ (%) (6)	RM (rad m <sup>-2</sup> ) (7)
1	325.81	+1.08	9.7	616.6	1.6	-23 ± 11
2	325.93	+2.92	4.6	51.1	9.0	-159 ± 28
3	325.96	+3.14	6.2	357.1	1.7	-172 ± 20
4	326.30	+2.17	10.4	234.0	4.4	-357 ± 10
5	326.54	+2.18	7.2	23.5	30.6	-505 ± 14
6	326.80	+1.57	14.3	226.4	6.3	-768 ± 8
7	326.94	+2.40	3.5	128.8	2.7	-808 ± 29
8	327.31	+0.88	6.8	288.5	2.4	-156 ± 16
9	327.52	+2.70	6.8	64.9	10.5	-595 ± 16
10	327.82	+1.29	7.3	92.6	7.9	-882 ± 14
11	327.87	+1.60	5.4	122.0	4.4	-818 ± 21
12	327.99	+1.48	3.3	154.0	2.1	-1344 ± 27
13	328.60	+3.05	6.0	136.3	4.4	-326 ± 18
14	328.62	+1.52	3.8	63.6	6.0	-933 ± 30
15	328.80	+2.80	4.6	85.9	5.4	-350 ± 25
16	329.20	+2.83	9.9	57.3	17.4	-348 ± 11
17	330.35	+1.81	3.3	89.9	3.7	+25 ± 35
18	330.56	+1.74	10.3	159.4	6.5	+4 ± 11
19	330.69	+1.63	3.9	12.3	32.0	+145 ± 25
20	330.77	+2.92	22.1	297.3	7.4	+172 ± 5
21	332.14	+1.03	9.4	140.0	7.1	-762 ± 12

FIG. 1.— Total intensity,  $I$ , in the SGPS Test Region. The greyscale runs from  $-30$  to  $+120$  mJy beam $^{-1}$ . The RMS in regions devoid of emission is 1.0–1.5 mJy beam $^{-1}$ .

FIG. 2.— Total intensity,  $I$ , in the SGPS Test Region as seen by the 2.4 GHz single dish survey of Duncan et al. (1995). The resolution is  $10''.4$  and the greyscale runs from  $-0.2$  to  $+17$  Jy beam $^{-1}$ , using a square-root transfer function to better show faint structure. The data shown here correspond to the “small-scale” image of Duncan et al. (1995), in which the largest scale structure has been filtered out.

FIG. 3.— Linearly polarized intensity,  $L = (Q^2 + U^2)^{1/2}$ . The greyscale runs from 0.4 to 9.5 mJy beam $^{-1}$ .

FIG. 4.— As in Fig 3, but with a greyscale range 1.0 to 5.0 mJy beam<sup>-1</sup>. The labeled ellipses delineate the approximate extents of voids 1 and 2, while the box shows the region of the field over which the profile shown in Fig 13 was generated.

FIG. 5.— Position angle (averaged across the band) of linearly polarized intensity  $\Theta = \frac{1}{2} \tan^{-1}(U/Q)$ . The values of the position angles have been converted from equatorial to Galactic coordinates, so that  $\Theta = 0^\circ$  represents a vector pointing in the direction of increasing  $b$  (i.e. up), and  $\Theta$  increases in the direction of increasing  $l$  (i.e. counter-clockwise). The greyscale runs from  $-40^\circ$  to  $+115^\circ$ .

FIG. 6.— Linearly polarized intensity,  $L$ , as seen by the 2.4 GHz single dish survey of Duncan et al. (1997a), covering the same part of the sky as in the SGPS Test Region. The resolution is  $10''.4$  and the greyscale runs from  $+1$  to  $+360$  mJy beam<sup>-1</sup>.

FIG. 7.— Distribution of rotation measure across the SGPS Test Region. The filled and open boxes represent positive and negative RMs respectively. For  $|\text{RM}| < 150$  rad m<sup>-2</sup>, the length of the side of each box is proportional to the RM at that position; for RMs of larger magnitudes, the boxes drawn correspond to  $|\text{RM}| = 150$  rad m<sup>-2</sup>. At positions where no box is shown, an RM could not be calculated either due to insufficient signal-to-noise or a poor fit to the position angles; RMs were also blanked at positions corresponding to polarized point sources. Each RM shown corresponds to the average over a  $15 \times 15$  pixel region (i.e.  $5' \times 5'$ ); only every second such RM along each axis is plotted. The background image represents the linearly polarized intensity from the Test Region as in Figs 3 and 4, but with a greyscale range of 0.2 to 19.0 mJy beam<sup>-1</sup>.

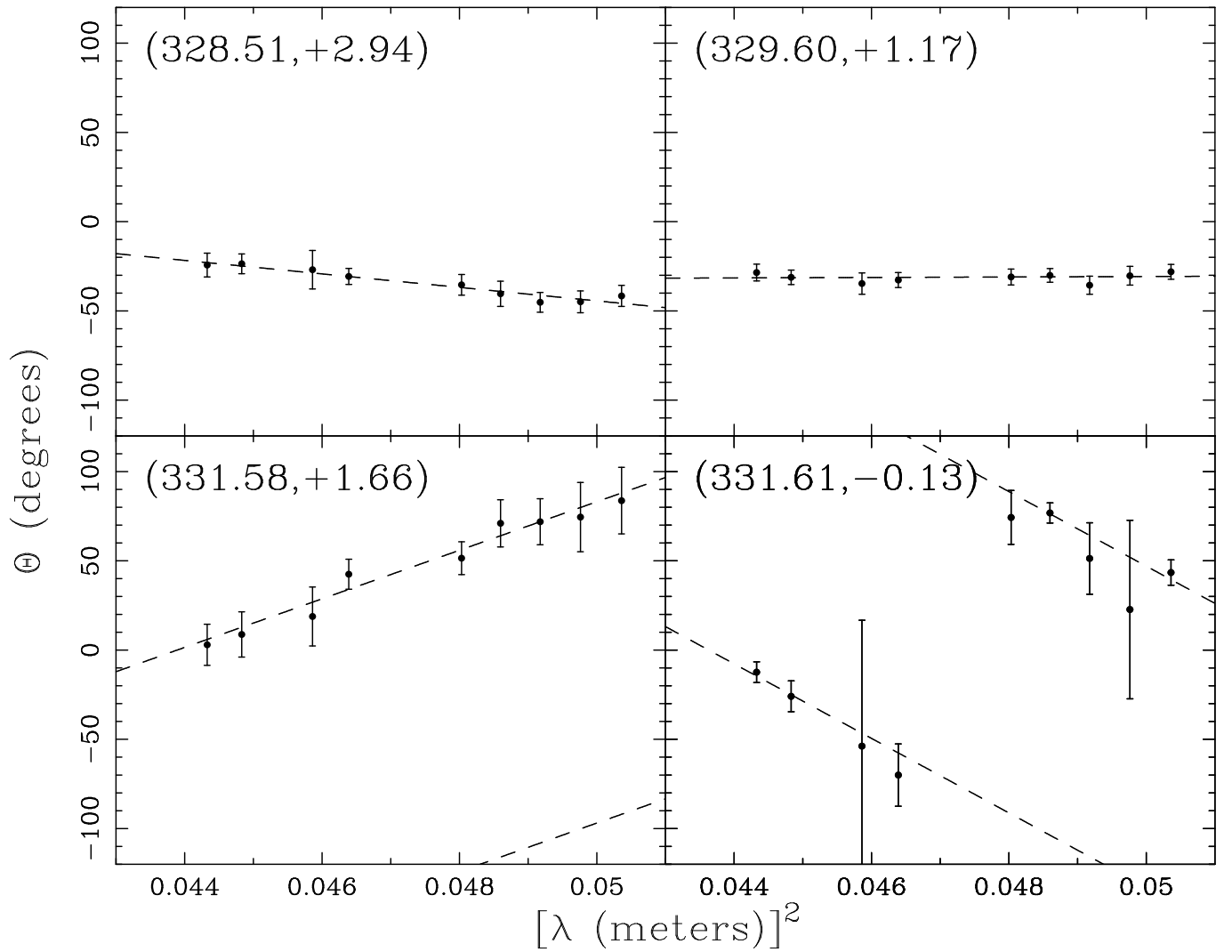


FIG. 8.— Plots of polarization position angle,  $\Theta$ , against  $\lambda^2$  towards four regions of diffuse polarization; the coordinates at which each measurement was taken are indicated in the upper left corner of each panel. The dashed line represents the least-squares fit to the data of the function  $\Theta = \Theta_0 + \text{RM} \lambda^2 + n\pi$ , where  $n = 0, \pm 1, \pm 2, \dots$ ; the corresponding values of RM are (ordered by increasing Galactic longitude)  $-66 \pm 17$ ,  $+2 \pm 13$ ,  $+237 \pm 39$  and  $-364 \pm 23 \text{ rad m}^{-2}$ . Note that the position angles shown here are relative to equatorial, rather than Galactic coordinates; this has no effect on the resultant RMs.



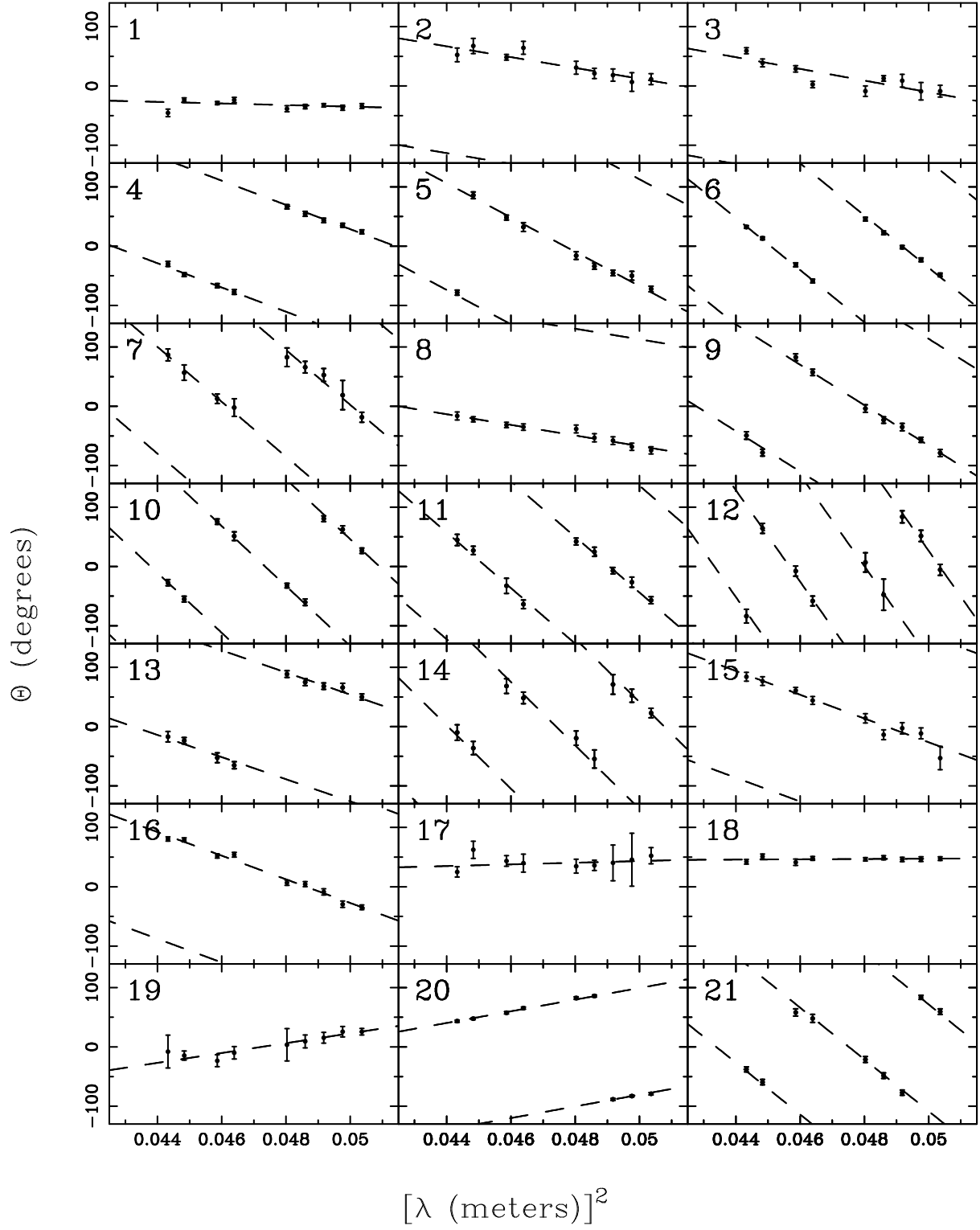


FIG. 9.— Plots of polarization position angle against  $\lambda^2$  for the 21 compact sources showing linear polarization as listed in Table 1. Details of the plots are as in Fig 8.

FIG. 10.— Polarized emission in the vicinity of the HII regions RCW 94 (upper right) and G326.7+0.5 (lower left). The greyscale represents linearly polarized intensity, while the single contour corresponds to total intensity emission from the same region at the level of  $45 \text{ mJy beam}^{-1}$ . The near-horizontal line corresponds to the intensity slice shown in Fig 11.

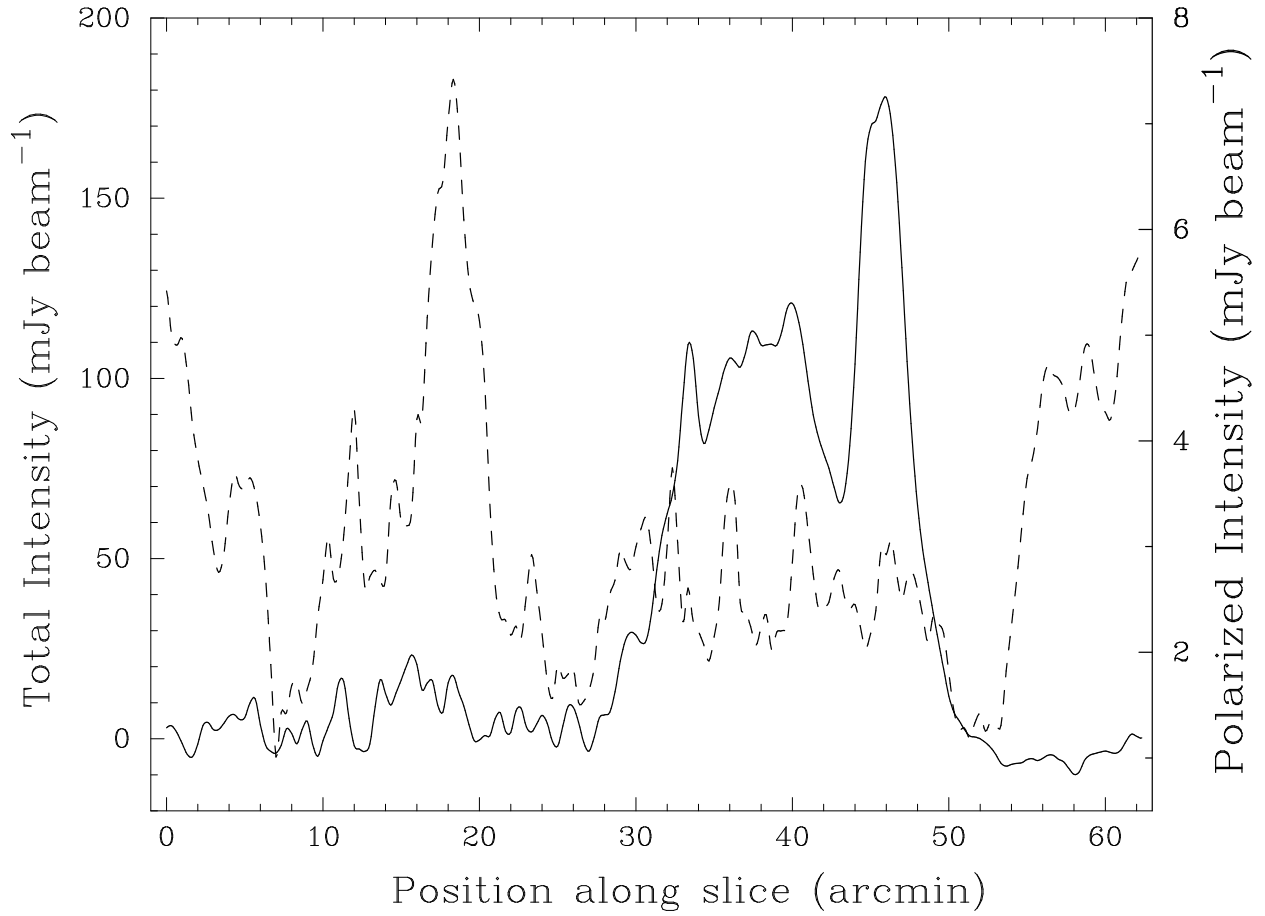


FIG. 11.— Profiles of total intensity (solid line) and linearly polarized intensity (broken line) across RCW 94. The slice along which these profiles was taken is shown in Fig 10.

FIG. 12.— Polarization properties of “canals” in a small part of the Test Region. The greyscale represents polarized position angle, while the contours (at levels of 3, 3.5 and  $4 \text{ mJy beam}^{-1}$ ) indicate polarized intensity. The boxes represent rotation measure as in Fig 7; here the largest boxes shown correspond to RMs of magnitude greater than  $\pm 30 \text{ rad m}^{-2}$ . It can be seen that the position angle sharply changes across each canal, but that there are no corresponding changes in RM.

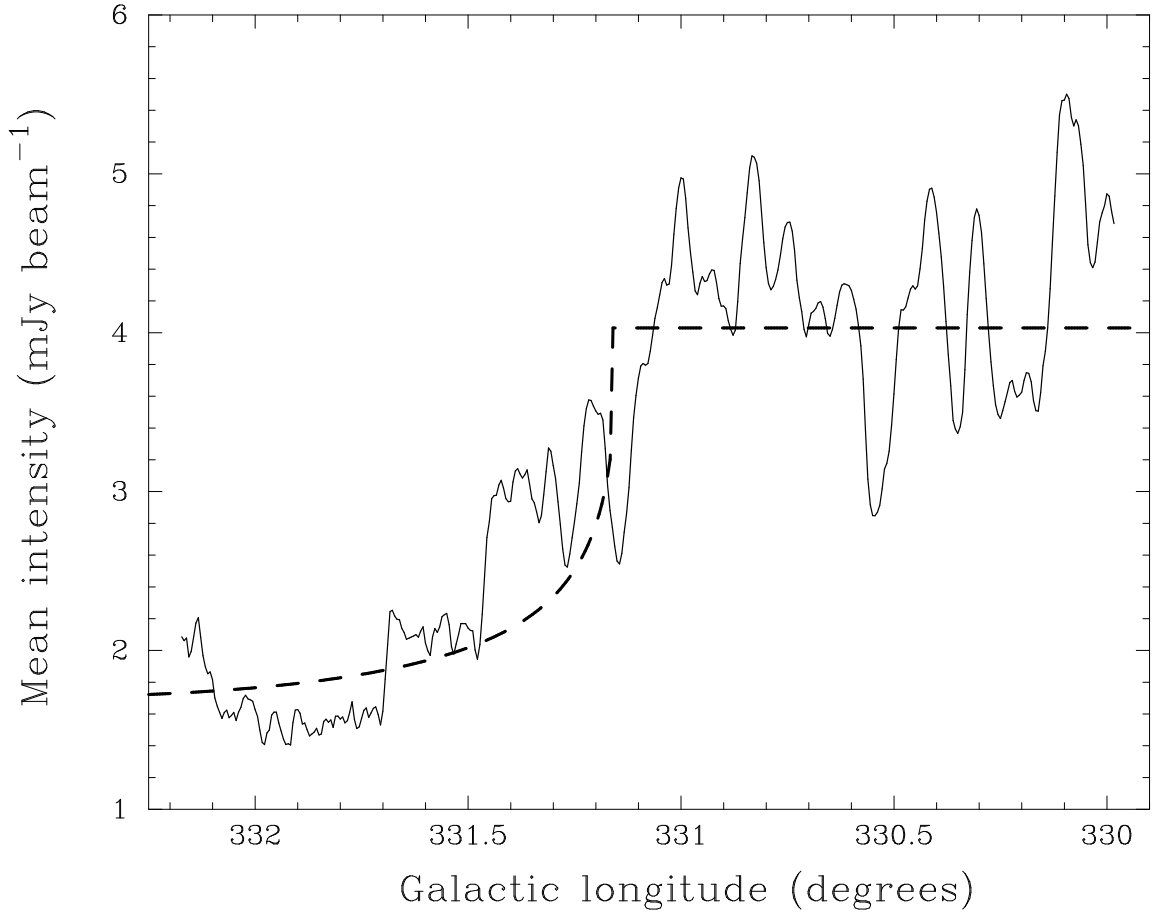


FIG. 13.— Profile of polarized intensity as a function of longitude across void 1, covering the region marked with a box in Fig 4. The solid line represents the mean polarized intensity of the data averaged over the range  $0^{\circ}.7 < b < 1^{\circ}.2$ . The dashed curve is the depolarization predicted by Equation (11), resulting from RM fluctuations on scales of 1 arcmin with dispersion  $\sigma_{\text{RM}} = 37 \text{ rad m}^{-2}$ .

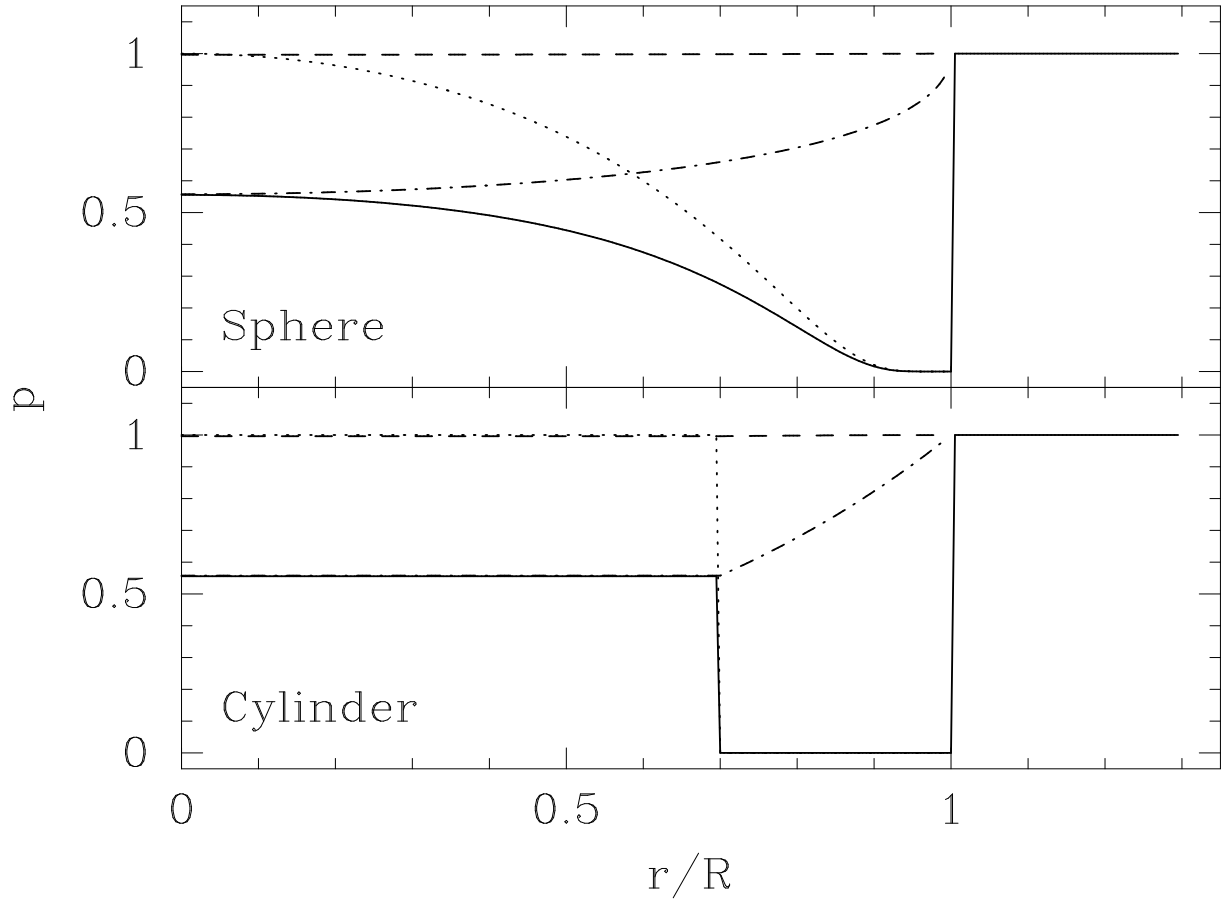


FIG. 14.— Predicted depolarization factor as a function of distance from the center of RCW 94, for spherical (upper) and cylindrical (lower) geometries. In both cases the parameters assumed were  $2R = 28$  pc,  $n_e = 20$  cm $^{-3}$ ,  $B_\theta = B_r = 1.2$   $\mu$ G,  $l = 0.15$  pc and  $\theta = 60^\circ$ . The dashed, dotted and dot-dashed lines correspond respectively to bandwidth ( $p_b$ ; Equation [4]), RM-gradient ( $p_g$ ; Equation [5]) and beam depolarization ( $p_f$ ; Equation [11]). The solid line represents the total depolarization ( $p$ ; Equation [14]).

## APPENDIX

## EFFECT OF AN INTERFEROMETER ON MEASURED ROTATION MEASURE

Suppose that there is a background source of emission, with uniformly polarized intensity  $P_0$  and uniform polarization position angle  $\Theta_0$ . The complex polarization corresponding to such a source is:

$$\mathbf{P}_0 = P_0 e^{2i\Theta_0}, \quad (\text{A1})$$

so that  $Q_0 = P_0 \cos 2\Theta_0$  and  $U_0 = P_0 \sin 2\Theta_0$ . This emission passes through a uniform screen of rotation measure  $R_s$ , and then through a compact cloud of rotation measure  $R_c$ .

After passing through the uniform screen, the resultant complex polarization is:

$$\mathbf{P}_s = \mathbf{P}_0 e^{2iR_s\lambda^2} = P_0 e^{2i(\Theta_0+R_s\lambda^2)} \quad (\text{A2})$$

Along lines-of-sight which then pass through the cloud, the complex polarization is:

$$\mathbf{P}_c = \mathbf{P}_s e^{2iR_c\lambda^2} = P_0 e^{2i(\Theta_0+R_s\lambda^2+R_c\lambda^2)} \quad (\text{A3})$$

Suppose that this radiation field is then observed with an interferometer. The interferometer is only sensitive to a limited range of spatial scales (which we assume includes that corresponding to the extent of the compact cloud), but has no sensitivity to the uniform component of the emission. Thus the emission detected by the instrument is the incident field, less the uniform component.

Thus on lines-of-sight which do not pass through the cloud, the detected complex polarization is:

$$\mathbf{P}_{\text{det}} = \mathbf{P}_s - \mathbf{P}_s = 0, \quad (\text{A4})$$

indicating that no emission is detected off-source. However, towards the cloud, one detects:

$$\mathbf{P}_{\text{det}} = \mathbf{P}_c - \mathbf{P}_s = P_0 e^{2i(\Theta_0+R_s\lambda^2)} \left( e^{2iR_c\lambda^2} - 1 \right). \quad (\text{A5})$$

This simplifies to:

$$\mathbf{P}_{\text{det}} = 2P_0 \sin(R_c\lambda^2) e^{2i\left(\Theta_0 + \frac{\pi}{4} + \lambda^2 \left[ R_s + \frac{R_c}{2} \right]\right)}, \quad (\text{A6})$$

so that we can write:

$$\mathbf{P}_{\text{det}} = P_{\text{det}} e^{2i(\Theta_{\text{det}} + \text{RM}_{\text{det}}\lambda^2)}, \quad (\text{A7})$$

where  $P_{\text{det}} = 2P_0 \sin(R_c\lambda^2)$ ,  $\Theta_{\text{det}} = \Theta_0 + \frac{\pi}{4}$  and  $\text{RM}_{\text{det}} = R_s + \frac{R_c}{2}$ .

Thus when observed with an interferometer, no polarized emission is seen on lines-of-sight which do not pass through the cloud, since this uniform component of the polarized emission is completely resolved out by the interferometer. Towards the cloud, polarized emission is detected, but whose apparent polarized intensity can be as large as twice that of the emitting source. The RM measured towards this emission is the sum of the RM from the diffuse component and *half* the RM of the cloud. After correction for Faraday rotation, the intrinsic position angle of incident radiation inferred from the observations is  $45^\circ$  greater than the true position angle of the emitted radiation.

This figure "fig01.jpg" is available in "jpg" format from:

<http://arxiv.org/ps/astro-ph/0010518v1>

This figure "fig02.jpg" is available in "jpg" format from:

<http://arxiv.org/ps/astro-ph/0010518v1>

This figure "fig03.jpg" is available in "jpg" format from:

<http://arxiv.org/ps/astro-ph/0010518v1>



This figure "fig04.jpg" is available in "jpg" format from:

<http://arxiv.org/ps/astro-ph/0010518v1>

This figure "fig05.jpg" is available in "jpg" format from:

<http://arxiv.org/ps/astro-ph/0010518v1>

This figure "fig06.jpg" is available in "jpg" format from:

<http://arxiv.org/ps/astro-ph/0010518v1>

This figure "fig07.jpg" is available in "jpg" format from:

<http://arxiv.org/ps/astro-ph/0010518v1>

This figure "fig10.jpg" is available in "jpg" format from:

<http://arxiv.org/ps/astro-ph/0010518v1>

This figure "fig12.jpg" is available in "jpg" format from:

<http://arxiv.org/ps/astro-ph/0010518v1>